International Journal of Nanomedicine

Dovepress
Taylor & Francis Group

Open Access Full Text Article

ORIGINAL RESEARCH

RGD-Modified Gold Nanoparticles Loaded with SAHA Remodel the Hypoxic Inflammatory Microenvironment via Inhibiting HIF-1α-VEGF Signaling to Enhance Radiosensitivity in NSCLC

Junqi Lin[1,*], Xiaoming Huang[1,*], Xizhen Wang[1], Ruilin Yu[1], Jie Liang[1], Rui Song[1], Wenbiao Chen[2], Guanle Shen[1]

[1]Department of Respiratory Medicine, People's Hospital of Longhua Shenzhen, Shenzhen, 518109, People's Republic of China; [2]Department of Gastroenterology, Shenzhen People's Hospital, The Second Clinical Medical College, Jinan University; The First Affiliated Hospital, Southern University of Science and Technology, Shenzhen, 518020, People's Republic of China

*These authors contributed equally to this work

Correspondence: Guanle Shen, Department of respiratory medicine, People's Hospital of Longhua Shenzhen, No. 38, Jinglong Construction Road, Longhua District, Shenzhen, Guangdong, 518109, People's Republic of China, Tel +86 0755 29572571, Email shenguanlelh@163.com; Wenbiao Chen, Department of Gastroenterology, Shenzhen People's Hospital, The Second Clinical Medical College, Jinan University; the First Affiliated Hospital, Southern University of Science and Technology, Shenzhen, 518020, People's Republic of China, Tel +86 0755 25533018, Email chanwenbiao@sina.com

Objective: This research explored the effectiveness of RGD peptide-functionalized gold nanoparticles (AuNPs) loaded with the histone deacetylase inhibitor SAHA (suberoylanilide hydroxamic acid) to enhance the radiosensitivity of non-small cell lung cancer (NSCLC) by suppressing hypoxia signaling, thereby mitigating oxidative stress and inflammatory responses.

Methods: RGD-AuNPs-SAHA was synthesized via citrate reduction, thiol-gold bonding for RGD modification, and SAHA loading. Structural and chemical characteristics were assessed via dynamic light scattering (DLS), transmission electron microscopy (TEM), UV-Vis spectroscopy, high-performance liquid chromatography (HPLC), Fourier-transform infrared spectroscopy (FTIR), thermogravimetric analysis (TGA), and X-ray photoelectron spectroscopy (XPS). Elemental distribution was mapped using TEM-EELS. Drug release behavior was evaluated under neutral and acidic conditions (pH 7.4 and 5.5). SAHA release kinetics were assessed at pH 7.4 and 5.5. Cellular uptake and biodistribution were evaluated in A549 cells and xenograft mice using fluorescence labeling and flow cytometry. Therapeutic efficacy was examined via tumor volume measurement, serum cytokine profiling (TNF-α, IL-6, IL-10), oxidative stress markers (SOD, CAT, MDA), and molecular analyses (IHC, IF, Western blot, RT-PCR). DNA damage and apoptosis were quantified using TUNEL and γ-H2AX staining.

Results: RGD-AuNPs-SAHA exhibited uniform size (~20 nm), high SAHA encapsulation (85.2%), and pH-responsive release (60% at pH 5.5 vs 35% at pH 7.4). XPS and EELS mapping further verified the formation of Au–S bonds between thiol-modified RGD and the AuNP surface. Quantitative analysis of surface-bound RGD peptides was performed using UV-Vis spectroscopy combined with the Levenberg–Marquardt algorithm. In vivo, RGD-AuNPs-SAHA reduced tumor volume by 60% and modulated inflammatory cytokines (↓TNF-α/IL-6, ↑IL-10). Oxidative stress markers improved significantly (SOD: 110 U/mL; CAT: 85 U/mL; MDA: ↓2 nmol/mL). Hypoxia signaling proteins HIF-1α and VEGF decreased by 50% and 40%, respectively, confirmed by Western blot and RT-PCR. Apoptosis and DNA damage markers increased by 70% (TUNEL) and 65% (γ-H2AX), demonstrating enhanced radiosensitization.

Conclusion: RGD-AuNPs-SAHA effectively remodeled the hypoxic tumor microenvironment, attenuated oxidative stress, and suppressed pro-tumorigenic signaling, leading to significant apoptosis and DNA damage. These findings highlight its potential as a radiosensitizer for NSCLC, offering a promising strategy to improve radiation therapy outcomes.

Keywords: gold nanoparticles, RGD peptide, hypoxic microenvironment, radiosensitivity, non-small cell lung cancer

Received: 1 April 2025
Accepted: 9 October 2025
Published: 10 December 2025

Introduction

Non-small cell lung cancer (NSCLC) is one of the most prevalent malignancies worldwide, accounting for approximately 85% of all lung cancer cases. Its high incidence and mortality rates make it a significant global healthcare challenge.[1,2] Although advances in surgical techniques, targeted therapies, and immunotherapies have improved the prognosis of NSCLC patients in recent years, a considerable number of cases are still detected at advanced stages, precluding surgical resection.[3,4] In such cases, radiotherapy (RT) is widely used in the clinical management of NSCLC, particularly for patients who cannot undergo surgery.[5,6] However, the effectiveness of RT is often constrained by several factors, particularly the heterogeneity of tumor tissues and their unique microenvironment, which can result in reduced sensitivity to RT in some patients, thereby limiting therapeutic outcomes.[7] Therefore, enhancing radiosensitivity, especially through modulation of the tumor microenvironment, has become a key focus of recent cancer treatment research.

Tumor hypoxia represents a major obstacle to the efficacy of RT, significantly impairing treatment outcomes.[8,9] Inadequate angiogenesis and abnormal blood circulation within tumor tissues often result in localized hypoxia.[10] This hypoxic state not only activates hypoxia-inducible factor (HIF), which enhances tumor invasiveness and drug resistance by regulating multiple signaling pathways but also inhibits the production of oxygen free radicals generated by radiation, reducing DNA damage in tumor cells.[11,12] Specifically, under hypoxic conditions, HIF-1α remains stable and activates downstream target genes, such as vascular endothelial growth factor (VEGF), further promoting angiogenesis and tumor cell survival.[13] Additionally, hypoxia alters the metabolic pathways of tumor cells, encouraging anaerobic glycolysis to provide the energy needed for their survival.[14] These factors collectively contribute to tumor resistance to RT. Therefore, targeting tumor hypoxia to enhance radiotherapeutic response has become a central theme in current cancer research.

With the rapid development of nanotechnology, gold nanoparticles (AuNPs) have garnered significant attention in cancer therapy due to their unique physicochemical properties. AuNPs exhibit excellent biocompatibility, chemical stability, and flexible surface modification capabilities, enabling precise targeting through various delivery methods.[15–17] In particular, AuNPs not only serve as drug delivery platforms but also enhance the tumor's response to external treatments, acting as an adjuvant to increase therapeutic efficacy.[18] For instance, AuNPs demonstrate excellent radiosensitizing properties in RT by increasing X-ray absorption at tumor sites, thereby enhancing the cytotoxic effects on tumor cells. Additionally, functional surface modifications, such as the incorporation of RGD peptides with targeting capabilities, can further improve the uptake efficiency and specificity of AuNPs in tumor cells.[19] With rapid advancements in nanotechnology, AuNPs have emerged as versatile carriers for anticancer agents, contributing to the evolution of multifunctional therapeutic strategies.

Histone deacetylases (HDACs) are key epigenetic regulators involved in gene transcription and diverse cellular processes. Suberoylanilide hydroxamic acid (SAHA), a clinically approved HDAC inhibitor, has demonstrated broad antitumor activity and has been utilized in the management of multiple cancer types in recent years.[20,21] By inhibiting HDAC activity, SAHA increases the acetylation levels of both histone and non-histone proteins in tumor cells, leading to apoptosis, reduced proliferation, and enhanced sensitivity to other therapeutic interventions.[22] Notably, SAHA has demonstrated radiosensitizing potential by altering DNA repair mechanisms and inhibiting tumor cell survival pathways.[23] However, the clinical application of SAHA remains limited due to its unfavorable pharmacokinetics and systemic toxicity. To overcome these challenges, recent studies have explored the use of nanotechnology to conjugate SAHA with AuNPs, aiming to achieve targeted delivery, increase tumor accumulation, and enhance therapeutic efficacy.

In this context, the current study focuses on constructing RGD peptide-modified gold nanoparticles loaded with suberoylanilide hydroxamic acid (RGD-AuNPs-SAHA) to explore its role in remodeling the hypoxic microenvironment of NSCLC and enhancing RT sensitivity. By modifying the nanoparticles with RGD peptides, the complex is expected to specifically target NSCLC cells and precisely deliver SAHA to tumor sites, thereby enhancing its antitumor efficacy. A comprehensive set of in vitro and in vivo experiments was performed to assess the effects of RGD-AuNP-SAHA on regulating hypoxic signaling pathways, reducing oxidative stress, and promoting tumor cell apoptosis, as well as its potential to improve RT sensitivity. The findings from this study provide a novel nanodrug delivery system for cancer therapy and hold promise for more precise and effective treatment strategies for NSCLC patients in future clinical applications. In addition to revealing the potential molecular mechanisms of SAHA-loaded AuNPs, this study offers

valuable theoretical insights and technical support for future cancer treatments, highlighting its significant scientific and clinical implications.

Materials and Methods

Synthesis of AuNPs

Gold nanoparticles (AuNPs) were prepared via the classical citrate reduction method. A 0.01 M solution of chloroauric acid ($HAuCl_4 \cdot 3H_2O$, Sigma-Aldrich, USA) was freshly prepared in deionized water. Fifty milliliters of this chloroauric acid solution were placed in a beaker and heated to 100°C until boiling. While the solution was boiling, 5 mL of 1% sodium citrate solution (Sigma-Aldrich, USA) was quickly added. Sodium citrate acts as a reducing agent, converting the gold ions (Au^3+) in the chloroauric acid to AuNPs. The solution was continuously heated and stirred for approximately 15 minutes until its color gradually changed from colorless or pale yellow to red, indicating the formation of AuNPs. The reaction mixture was then allowed to cool to ambient temperature and stored at 4 °C until further use.

Preparation of Peptide-Modified Gold Nanoparticles (RGD-AuNPs)

RGD-AuNPs were synthesized by conjugating thiol-modified RGD peptides to the surface of AuNPs. Thiol-modified RGD peptides (Peptide 2.0 Inc., USA) were dissolved in deionized water to prepare a 1 mM solution. The prepared AuNPs solution was mixed with the 1 mM RGD peptide solution at a 10:1 volume ratio. The mixture was stirred at ambient temperature for 12 hours to allow the thiol-modified RGD peptides to bind to the surface of the AuNPs. After the reaction, the mixture was centrifuged at 12,000 rpm for 20 minutes to remove unbound RGD peptides. The resulting pellet was collected and resuspended in deionized water. This washing process was repeated three times to ensure the purity of the peptide-modified AuNPs, with each cycle involving centrifugation (12,000 rpm, 20 minutes) and resuspension in deionized water.

Preparation of RGD-AuNPs-SAHA Complex

SAHA (Selleck Chemicals, USA) was dissolved in DMSO to prepare a 10 mM stock solution. The 10 mM stock solution was diluted with deionized water to obtain a 1 mM working solution. The 1 mM SAHA working solution was added to the RGD-AuNPs solution at a 1:10 ratio (SAHA working solution: RGD-AuNPs solution). The mixture was stirred at ambient temperature for 6 hours to allow SAHA to fully bind to the RGD-AuNPs. The resulting mixture was centrifuged (12,000 rpm, 20 minutes) to remove unbound SAHA. The pellet obtained after centrifugation was resuspended in deionized water. This washing step was repeated three times to ensure the purity of the RGD-AuNPs-SAHA complex, with each cycle involving centrifugation (12,000 rpm, 20 minutes) and resuspension in deionized water.

Particle Size and Morphology Characterization

The hydrodynamic diameter, surface charge, and structural morphology of the RGD-AuNPs-SAHA complexes were assessed using dynamic light scattering (DLS) and transmission electron microscopy (TEM). Briefly, the nanoparticle suspension was diluted with deionized water to a final volume of 1 mL. The average particle size and zeta potential were then determined using a Zetasizer Nano ZS instrument (Malvern Instruments, UK). For TEM observation, a drop of the diluted sample was deposited onto a carbon-coated copper grid (Ted Pella Inc., USA), followed by ambient air drying. Imaging was performed using a Transmission Electron Microscope (JEM-2100, JEOL Ltd., Japan).

Chemical Element Composition and Spatial Resolution Analysis

To determine the chemical bonding states and spatial distribution of elements in the nanoparticles, we performed X-ray Photoelectron Spectroscopy (XPS) and Energy-Filtered Transmission Electron Microscopy (EELS) mapping. After drying, samples were loaded and analyzed using an XPS instrument (Thermo ESCALAB250Xi, USA). The spatial resolution and elemental analysis were calculated using the formula: $d(nm)=\{(0.16\lambda/\beta)^2+(Cc\Delta E/E0\beta)^2+(0.5Cs\beta^3)^2\}^{1/2}$, where γ is the wavelength, β is the collection angle, Cc is the chromatic aberration coefficient, ΔE is the energy width of the integrated intensity, and E_0 is the accelerating voltage.[24,25]

Quantitative Analysis of RGD Peptides on AuNPs

To quantify the RGD peptides conjugated on AuNP surfaces, XPS-based deconvolution of the UV–Vis absorption spectrum was performed. The absorption spectrum of the sample was imported as a text file and the X-axis was reversed to match the UV–Vis spectral direction. The region of interest was selected and the background was set as linear. Peak deconvolution was performed by identifying constituent peaks using the LN-MIE-Gans (Levenberg-Marquardt) fitting algorithm.[26] This analysis confirmed the binding between RGD peptides and AuNPs.

Determination of Encapsulation Efficiency and Loading Capacity

The encapsulation efficiency and drug loading capacity of SAHA were evaluated using both ultraviolet-visible (UV-Vis) spectrophotometry and high-performance liquid chromatography (HPLC). The UV-Vis spectrophotometer (Lambda 25, PerkinElmer, USA) was used to scan the samples across a wavelength range of 200–800 nm to identify the characteristic absorption peaks of SAHA. For quantitative analysis, samples were analyzed on an HPLC system (Agilent 1260 Infinity, Agilent Technologies, USA) equipped with a C18 column (4.6 mm × 250 mm, 5 μm; Agilent Technologies). The mobile phase consisted of acetonitrile and water in a 60:40 (v/v) ratio, delivered at a flow rate of 1.0 mL/min. Detection was conducted at 254 nm to quantify the amount of SAHA encapsulated within the nanoparticles.

Confirmation of SAHA Loading Efficiency and Nanoparticle Stability

To verify the loading efficiency of SAHA and the stability of the nanoparticles, Fourier Transform Infrared Spectroscopy (FTIR) and Thermogravimetric Analysis (TGA) were employed. After preparing the sample using the KBr pellet method, the FTIR spectra were recorded in the 4000–400 cm^{-1} range using a Nicolet iS10 spectrometer (Thermo Fisher Scientific, USA). For TGA, the samples were analyzed under a nitrogen atmosphere using a TGA 4000 analyzer (PerkinElmer, USA) over a temperature range of 25–800°C, with a heating rate of 10°C/min.

Evaluation of Drug Release Behavior

To assess the release behavior of SAHA from RGD-AuNPs, an in vitro drug release experiment was conducted. RGD-AuNPs-SAHA suspension was placed in a dialysis bag (MWCO 10 kDa, Spectrum Labs, USA) and incubated at 37°C in phosphate-buffered saline (PBS, pH 7.4) and acetate buffer (pH 5.5). Samples were collected at regular intervals, and the concentration of released SAHA was measured using UV-Vis spectrophotometry to determine the drug release kinetics.

Evaluation of Stability in Physiological Conditions

The colloidal stability of RGD-AuNPs-SAHA was assessed under simulated physiological conditions using DLS and TEM to monitor changes in particle size and morphology. Nanoparticle suspensions were incubated at 37 °C in buffer solutions adjusted to pH 7.4 and pH 5.5. Aliquots were collected at 6-hour intervals over a 24-hour period for subsequent characterization.

Observation of Cellular Uptake Experiment

To evaluate cellular internalization, AuNPs were labeled with fluorescein isothiocyanate (FITC; Sigma-Aldrich, USA). A 1 mM FITC stock was prepared in DMSO and added to the AuNP solution, followed by stirring at ambient temperature for 4 hours in the dark. Excess FITC was removed by centrifugation. A549 human NSCLC cells (ATCC, USA) were seeded on sterile glass coverslips and maintained in RPMI 1640 medium containing 10% Fetal Bovine Serum (FBS) (Gibco, USA) until reaching 80% confluence. The FITC-labeled AuNPs complexes were then incubated with the cells for 1, 2, and 4 hours. After incubation, cellular uptake and localization were observed using a confocal microscope (LSM 880, Zeiss, Germany).

Cell Culture and Treatment

Human alveolar epithelial cell line TT1 and human NSCLC cell lines A549 and Calu-1 were obtained from the American Type Culture Collection (ATCC, Rockville, MD). The cells were cultured in Dulbecco's Modified Eagle Medium

(DMEM, Gibco BRL, Carlsbad, CA), supplemented with 10% FBS (FBS, Gibco BRL, Carlsbad, CA), 100 units/mL penicillin, 100 μg/mL streptomycin, and 2 mM glutamine. Cultures were maintained in a humidified incubator at 37°C with 5% CO_2.

Cell Transfection

To evaluate the effect of HIF-1α overexpression on the treatment efficacy of RGD-AuNPs-SAHA, total RNA was extracted from A549 cells and reverse-transcribed into cDNA using reverse transcriptase (Thermo Fisher Scientific, USA). The HIF-1α gene sequence was amplified by PCR with specific primers. After verification of the PCR product through agarose gel electrophoresis, the amplified product was ligated into the pCDNA3.1 expression vector using a ligase (New England Biolabs, USA) to form a recombinant plasmid. The recombinant plasmid was extracted from Escherichia coli using a plasmid extraction kit (Qiagen, Germany) and confirmed by restriction enzyme digestion (New England Biolabs, USA) and sequencing (Genewiz, USA). The confirmed HIF-1α expression plasmid was introduced into A549 cells using Lipofectamine 3000 reagent (Thermo Fisher Scientific, USA). Transfected cells were cultured in RPMI-1640 medium supplemented with 10% fetal bovine serum (FBS; Gibco, USA) under standard incubation conditions (37 °C, 5% CO_2). After 48 hours, HIF-1α expression levels were quantified by RT-qPCR and Western blotting to assess the impact on hypoxia and cell viability. The primer sequences for HIF-1α (NCBI Reference Sequence: NM_001243084.2) overexpression were as follows: forward 5′-AGAGGTTGAGGGACGGAGAT-3′, reverse 5′-TTGTGGCTACCACGTACTGC-3′.

To confirm that the inhibitory effects of SAHA and RGD-AuNPs-SAHA are specifically mediated through the JAK2/STAT3 pathway, the JAK2/STAT3 phosphorylation enhancer Butyzamide (MCE, USA) was used. Cells were treated with 3 μM of Butyzamide, either alone or in combination with RGD-AuNPs-SAHA.

AuNPs Treatment and MTT Cytotoxicity Assay

TT1 cells in the logarithmic growth phase were seeded into 96-well plates (Falcon, BD Biosciences, USA) at a density of 1×10^5 cells per well and allowed to adhere overnight. Cells were then treated with either 50 μM of unloaded AuNPs, HDAC inhibitor SAHA, RGD-AuNPs, or RGD-AuNPs-SAHA for 24 and 48 hours. Each treatment group was tested in quadruplicate. Untreated cells served as the control group. Cell viability was assessed using the MTT assay, which evaluates metabolic activity via the enzymatic reduction of MTT to formazan. After treatment, MTT reagent was added, and the resulting formazan crystals were solubilized. Absorbance was measured at 570 nm using a SpectraMax 250 microplate reader (Molecular Devices, USA). Experiments were conducted in triplicate with four technical replicates per group. Viability was expressed as a percentage relative to the control group, which was defined as 100%.

Enzyme-Linked Immunosorbent Assay (ELISA)

TT1 cells from each experimental group (control, AuNP-only, SAHA, and RGD-AuNPs-SAHA) were seeded into 6-well plates at a density of ~2×10^5 cells/well and cultured for 24 hours. Supernatants were collected and centrifuged to remove residual cells and debris. Levels of IL-6 and IL-8 were quantified using commercially available ELISA kits (R&D Systems, USA). The procedure involved adding standards and samples to a 96-well plate pre-coated with antibodies, followed by incubation and washing. An enzyme-linked secondary antibody was then added, followed by substrate addition for colorimetric development. Absorbance was recorded at 450 nm using a microplate reader, and cytokine concentrations were calculated based on standard curves. All measurements were performed in triplicate to ensure reproducibility.

Vivo Biocompatibility

Animal experiments were conducted in accordance with the Animal Care and Use Guidelines of the Ethics Committee of People's Hospital of Longhua Shenzhen. Healthy male BALB/c nude mice, aged 6–8 weeks (catalog no. 401, Beijing Vital River Laboratory Animal Technology Co., Ltd., Beijing, China), were selected for the study. The mice were housed under a 12-hour light/dark cycle, with controlled temperatures between 22°C and 25°C and relative humidity maintained

at 50%-60%. They had free access to food and water. A one-week acclimation period was provided prior to the start of the experiments.

To evaluate the biocompatibility of HDAC inhibitor SAHA-loaded peptide-modified AuNPs in vivo, mice were intravenously administered 0.2 mL of AuNPs, RGD-AuNPs, or RGD-AuNPs-SAHA (50 mM) via the tail vein. PBS-treated animals served as controls. At defined time points post-injection, blood samples were collected for gold quantification using inductively coupled plasma mass spectrometry (ICP-MS). Urine and feces were simultaneously collected in metabolic cages, dried, digested in aqua regia, and analyzed for gold content by ICP-MS (n = 4 per group). At 24 hours post-administration, blood samples were also subjected to complete blood count and serum biochemical profiling. Pro-inflammatory cytokines, including IL-6 and TNF-α, were measured using ELISA kits (Abcam, UK). Mice were euthanized one day post-injection, and vital organs (heart, liver, spleen, lungs, kidneys) were harvested for histopathological assessment via hematoxylin and eosin (H&E) staining.

Vivo Clearance Kinetics of AuNPs

The experiment was conducted using male nude mice (n = 4) carrying in situ LM3 liver tumors. Each mouse received a 200 μL solution via tail vein injection. At various time points post-injection, blood samples were collected to measure gold concentrations using ICP-MS. Urine and feces were gathered at corresponding time points in metabolic cages, dried, digested with aqua regia, and subjected to ICP-MS for gold quantification.

At 24 hours post-injection, tumor tissues and major organs were harvested to determine nanoparticle accumulation. Tumors were isolated, weighed, and lyophilized. Dried tumor and organ samples were digested in aqua regia, diluted appropriately, and analyzed by ICP-MS to measure gold content and evaluate tissue-specific distribution of AuNPs.

Cell Viability Assay and Colony Formation Experiment

To evaluate cellular viability, Calu-1 and A549 cells from each treatment group (control, blank nanoparticles, SAHA, RGD-AuNPs, and RGD-AuNPs-SAHA) were seeded into 96-well plates at 5×10^3 cells per well. Cells were maintained in RPMI-1640 medium supplemented with 10% fetal bovine serum (FBS) at 37 °C in a 5% CO_2 atmosphere for 24 hours. Cell viability was assessed using a CCK-8 assay (Dojindo, Japan), by adding 10 μL of reagent to each well followed by a 2-hour incubation. Absorbance at 450 nm was measured using a microplate reader to quantify proliferation. Each experiment included three biological replicates with four technical replicates per group.

For the colony formation assay, A549 and Calu-1 cells were plated into 6-well plates at a density of 5×10^3 cells per well and cultured for 14 days under standard conditions in the presence of varying concentrations of anlotinib. After incubation, colonies were fixed and stained with 0.1% crystal violet for 30 minutes, followed by manual counting under a light microscope.

Cell Climbing Assay and TUNEL Staining

A549 cells from the control group, blank nanoparticle group, SAHA group, RGD-AuNPs group, and RGD-AuNPs-SAHA group were seeded onto glass coverslips and cultured until approximately 70% confluence was reached. The cells were then fixed with 4% paraformaldehyde for 15 minutes and washed three times with PBS. Subsequently, TUNEL staining was performed using a TUNEL staining kit (Roche, Switzerland). Stained samples were visualized using a fluorescence microscope (Leica Microsystems, Germany), where apoptotic nuclei emitted green fluorescence. The percentage of TUNEL-positive cells was calculated to quantify apoptosis. Each condition was analyzed in three independent experiments.

Flow Cytometry and Hoechst Staining for Apoptosis Detection

For flow cytometric detection of apoptosis, cells from all groups were harvested, washed twice with cold PBS, and resuspended in 200 μL of binding buffer. Annexin V-FITC (5 μL) and propidium iodide (5 μL) were added, and samples were incubated in the dark for 15 minutes at ambient temperature. Apoptotic populations were analyzed using a FACSCalibur flow cytometer (BD Biosciences, USA), with a minimum of 20,000 events recorded per sample. Experiments were repeated in triplicate.

For nuclear morphology assessment, cells were fixed with 4% paraformaldehyde for 10 minutes and stained with Hoechst 33342 (Beyotime, China) at 37 °C for 5 minutes in the dark. Fluorescent images were captured using a Nikon fluorescence microscope to identify apoptotic nuclei.

Scratch Assay

To evaluate cell migration ability, a scratch assay was performed. A549 cells were seeded in a 6-well plate at a density of approximately 2×10^5 cells per well and cultured until 90% confluence. A sterile pipette tip was used to generate a vertical scratch across the monolayer. Detached cells were removed by rinsing twice with PBS. Cells were then treated with a culture medium containing 50 μM SAHA, AuNPs, RGD-AuNPs, or RGD-AuNPs-SAHA, followed by incubation in a serum-free medium for 24 hours. Images of the wound area were captured at 0 and 24 hours, and the wound width was measured under a microscope. Cell migration ability was assessed by comparing the wound closure at 0 and 24 hours. The experiment was repeated three times to ensure data accuracy and consistency.

Transwell Invasion Assay

To examine cellular invasiveness, a Matrigel-coated Transwell system (Corning, USA) was used. A549 cells previously subjected to different treatments were suspended in serum-free medium and seeded into the upper chambers at 1×10^5 cells per 200 μL. The lower chambers contained 600 μL of medium with 10% FBS to serve as a chemoattractant. After 24 hours of incubation at 37 °C, non-invading cells on the upper membrane surface were removed. Cells that had migrated to the underside were fixed with methanol, stained with 0.1% crystal violet, and imaged under a light microscope for quantitative analysis.

RT-qPCR

Total RNA was extracted from treated cells using Trizol reagent (Invitrogen, USA), and first-strand cDNA was synthesized using a reverse transcription kit (Thermo Fisher Scientific, USA). Quantitative PCR (qPCR) amplification was then performed with SYBR Green Master Mix (Thermo Fisher Scientific, USA) on a real-time PCR system (Applied Biosystems, USA). The mRNA levels of HIF-1α (NCBI Reference Sequence: NM_001243084.2) and VEGF (NCBI Reference Sequence: NM_001025366.3) were measured. The primer sequences used for qPCR are listed in Table S1.

ELISA for Hypoxia-Related Protein Detection

To accurately measure the concentrations of HIF-1α and VEGF in human NSCLC cells, an ELISA kit from JONLNBIO (Shanghai, China) was used. In the experiment, cell culture supernatants were collected, followed by the sequential addition of the capture antibody from the ELISA kit and the target samples. Fluorescently labeled detection antibodies were then added to bind the specific proteins, enabling the quantification of HIF-1α and VEGF concentrations using the enzyme-linked immunosorbent technique. The absorbance of each sample was measured at a wavelength of 450 nm using a microplate reader (BioTek, USA) to obtain quantitative protein data.

Detection of Reactive Oxygen Species (ROS) Accumulation

To assess the levels of ROS in A549 cells, a ROS detection kit from Beyotime Biotechnology (Shanghai, China) was used. A549 cells were seeded at a density of 1×10^5 cells per 3.5 cm dish and incubated for 24 hours. Cells were then exposed to 0.1 μM SAHA, 6.8 μM AuNPs, RGD-AuNPs, RGD-AuNPs-SAHA, or 38 μM ATR for 12 hours. Following treatment, cells were harvested and incubated with 10 μL of DCFH-DA at 37 °C for 30 minutes in the dark. After staining, 300 μL of PBS was added, and fluorescence intensity reflecting ROS levels was measured using flow cytometry (BD Biosciences, USA).

Cell Cycle Analysis

A DNA quantification kit (Solarbio, Beijing, China) was used to analyze the cell cycle of A549 cells. A549 cells (1×10^5 cells per 3.5 cm dish) were cultured for 24 hours and then treated with 0.1 μM SAHA, 6.8 μM AuNPs, RGD-AuNPs, RGD-AuNPs-SAHA, or 38 μM ATR for 12 hours. After treatment, cells were fixed in 70% ethanol at 4 °C overnight. The

fixed cells were incubated with 100 μL RNase at 37 °C for 30 minutes, followed by staining with 400 μL PI for 30 minutes in the dark at 4 °C. Flow cytometry analysis was conducted to determine the percentage of cells in G0/G1, S, and G2/M phases.

Western Blot Analysis

Total protein was quantified using a BCA protein assay kit (Thermo Fisher Scientific, USA). Equal amounts of protein samples were separated by SDS-PAGE based on molecular weight. The proteins were then transferred onto PVDF or nitrocellulose membranes. To block nonspecific binding sites, the membranes were incubated with a blocking solution (eg, 5% non-fat milk). Primary antibodies, with β-actin (Cell Signaling Technology, USA) as the internal control, were used for incubation. HRP-conjugated secondary antibodies were applied, followed by the addition of an ECL chemiluminescent substrate to detect protein bands through an imaging system. Antibodies used in this experiment included those against phosphorylated JAK2 (p-JAK2), STAT3, phosphorylated STAT3 (p-STAT3), VEGF, Akt, phosphorylated Akt (p-Akt), CDK1/2, Cyclin B, p21, p27, HIF-1α, and VEGF, all purchased from Abcam (USA).

Construction of A549 Cell Xenograft Mouse Model

Human NSCLC A549 cells (ATCC, USA) were suspended in PBS and injected subcutaneously into the right axilla of 6-week-old female BALB/c nude mice (n=25, Charles River, USA) at a concentration of 1×10^7 cells/200μL.[27–29] All mice were housed under specific pathogen-free (SPF) conditions with free access to food and water. Tumor growth was monitored to assess therapeutic responses.

Processing of NSCLC Tissues and Organoid Culture

Primary NSCLC tumor tissue fragments (5–8 mm^3) were collected from early-stage patients undergoing surgical resection. Samples were immediately placed in ice-cold advanced DMEM (adDMEM) enriched with 10% FBS and 1% penicillin-streptomycin, and organoid culture was initiated within 20 minutes post-excision. Necrotic areas and non-tumor adjacent tissues were carefully trimmed away, and tumor samples were rinsed three times with adDMEM+++ (adDMEM supplemented with HEPES, GlutaMAX™, Primocin, and amphotericin B). Tissues were then minced into fragments less than 1 mm^3 using sterile scissors.

Tissue fragments were digested in adDMEM+++ containing 5 mg/mL collagenase (Gibco), 0.1 mg/mL DNase I (Sigma-Aldrich), and 10 μM Y-27632 (a ROCK inhibitor, R&D Systems), and incubated at 37°C under intermittent agitation (200 rpm) for 1 hour. The digestion was stopped by adding adDMEM+++ with 10% FBS, followed by centrifugation at 200 × g for 3 minutes at 4°C. After washing, the cell pellet was filtered through a 70 μm strainer (BD Falcon, USA), recentrifuged, and resuspended in a 1:1 mixture of growth factor-reduced Matrigel (Corning, #354230) and adDMEM+++. The Matrigel-cell suspension (20 μL per well) was plated in the center of each well of a 24-well plate and allowed to polymerize by incubating the plate in an inverted position at 37 °C for 20 minutes.

After polymerization, each well received NSCLC organoid medium composed of adDMEM+++ supplemented with human EGF, FGF, Noggin, SB202190, B27, N2, and Y-27632. Medium was refreshed every four days. Organoid passage was performed when more than 50% of the patient-derived tumor organoids (PDTOs) reached a diameter of at least 100 μm, typically within 1–2 weeks. Organoids were then characterized, cryopreserved, or used for drug testing.

Growth time was defined as the interval between initial seeding and the point when over 50% of PDTOs exceeded 100 μm in diameter. Doubling time was calculated as the period required for organoids to occupy the full area of the Matrigel dome. PDTOs were maintained for at least four passages prior to cryostorage. For long-term storage, organoids were preserved in a freezing solution containing 10% dimethyl sulfoxide (DMSO) in FBS, forming a viable organoid biobank.

Organoids were successfully re-established from both cryopreserved primary lung cancer tissue and previously frozen PDTOs, maintaining a 100% recovery rate. These results align with previous reports indicating organoid revival rates greater than 70%.[30]

Experimental Grouping and Drug Administration

Mice were randomly divided into five groups (n = 5 per group): Control group (injected with an equivalent volume of saline), Blank Nanoparticle group (injected with blank RGD-AuNPs, 50 mg/kg), SAHA group (injected with free SAHA, 10 mg/kg), RGD-AuNPs group (injected with peptide-loaded AuNPs, 50 mg/kg), and RGD-AuNPs-SAHA group (injected with SAHA-loaded RGD-AuNPs, 10 mg/kg). All treatments were administered via tail vein injection once every other day for a total of four weeks.

Biodistribution Observation

To evaluate the biodistribution of nanoparticles in mice, fluorescently labeled RGD-AuNPs-SAHA were administered via tail vein injection. Nude mice (Balb/c, 6 weeks old, 20 g, Experimental Animal Center, USA) were divided into five groups, with each group receiving 0.2 mL of FITC-labeled AuNPs. The biodistribution of the nanoparticles was monitored at various time points (10 minutes, 30 minutes, 5 hours, and 24 hours) using an in vivo imaging system (IVIS Spectrum, PerkinElmer, USA).

Localized X-Ray Irradiation

Each group of mice received localized X-ray irradiation 24 hours following the final drug administration. Mice were anesthetized and subjected to tumor-targeted irradiation using a precision RT platform (Varian Medical Systems, USA). A single fraction dose of 6 Gy was delivered to the tumor region while minimizing exposure to surrounding tissues by applying customized shielding.

Tumor Volume and Body Weight Measurement

Tumor volume and body weight were measured every two days. Tumor dimensions, including the longest and shortest diameters, were determined using a caliper. Tumor volume was determined using the formula: Volume = (longest diameter × shortest diameter^2) / 2. The body weight of each mouse was recorded to assess therapeutic efficacy and systemic toxicity.

Serological Testing

At the conclusion of the experiment, a specific volume of blood was collected from the test animals via venipuncture. The blood samples were centrifuged to remove blood cells, yielding serum samples. These samples were sent to IDEXX BioResearch (USA), where multiple serum parameters were analyzed using advanced equipment and technology. Liver function was assessed by measuring enzyme levels, such as alanine aminotransferase (ALT) and aspartate aminotransferase (AST), and total bilirubin. Renal function was assessed through serum creatinine (CREA) and blood urea nitrogen (BUN) levels. Additionally, red blood cell, white blood cell, and platelet counts and morphology were examined to assess overall health and immune function (Table 1).

Serum Oxidative Stress Biomarker Detection

To assess the impact of RGD-AuNPs-SAHA on oxidative stress levels in mice and verify its inhibitory effect on the hypoxia signaling pathway, serum oxidative stress markers were measured. Blood samples were collected in

Table 1 Biochemical Parameters of Treated Mice

Group	BUN (mmol/L)	ALT (U/L)	AST (U/L)	ALB (g/L)	CREA (μM/L)	K (mmol/L)	NA (mmol/L)	Cl (mmol/L)	TP (g/L)	TC (mmol/L)	TG (mmol/L)
Control	6.64±0.73	59.07±4.49	115.50±10.14	0.99±0.05	38±6.45	10.82±0.15	156.52±11.32	45.27±1.64	25.97±5.04	1.16±0.12	0.61±0.06
AuNPs	6.98±0.86	63.51±4.47	105.59±9.84	1.12±0.04	37±7.32	11.40±0.46	143.01±5.21	43.46±2.05	26.17±3.17	1.45±0.29	0.64±0.05
RGD-AUNPs	6.57±0.79	58.68±8.36	112.87±11.25	16.63±1.48	38±5.24	10.91±0.02	152.04±7.88	43.08±3.63	25.16±5.16	1.16±0.27	0.61±0.04
SAHA	6.25±0.92	59.96±9.74	104.93±8.27	17.77±3.47*	39±8.55	10.95±0.12	151.66±6.22	48.74±3.05	27.15±4.59	1.80±0.86	0.57±0.01
RGD-AUNPs-SAHA	6.67±0.52	55.90±10.80	106.01±7.18	1.00±0.07	36±10.36	10.34±0.86	155.43±5.32	46.23±2.11	26.06±3.08	1.05±0.28	0.63±0.05

Notes: The results are expressed as mean ± standard deviation (SD), with n=4. *$P < 0.05$.

https://doi.org/10.2147/IJN.S531731

anticoagulant tubes and centrifuged at 3000 rpm for 10 minutes to separate the serum. Commercial assay kits were used to measure superoxide dismutase (SOD), catalase (CAT), and malondialdehyde (MDA) levels. The absorbance of the serum samples mixed with reagents was measured at specific wavelengths, and the SOD activity, CAT activity, and MDA concentration were calculated.

H&E Staining Analysis

After the experiment, the tumors and major organs (liver, kidney, heart, lung, and spleen) were fixed in 10% neutral buffered formalin (Sigma-Aldrich, USA) for 24 hours. The samples were then embedded in paraffin, and sections were cut at a thickness of 5 μm. The sections were stained with H&E (H&E, Thermo Fisher Scientific, USA), dehydrated, and mounted with neutral balsam (Sigma-Aldrich, USA). Histological morphology was examined under a light microscope (Olympus, Japan).

Immunohistochemistry (IHC) Staining

To assess the expression and distribution of HIF-1α and VEGF in tumor tissues, an IHC analysis was conducted. Paraffin sections were deparaffinized with xylene and rehydrated through a graded ethanol series. Antigen retrieval was performed in sodium citrate buffer (pH 6.0) using microwave heating. Endogenous peroxidase activity was blocked with 3% hydrogen peroxide (Sigma-Aldrich, USA) for 10 minutes. The sections were then blocked with 5% bovine serum albumin (BSA, Sigma-Aldrich, USA) for 1 hour. Primary antibodies for HIF-1α (1:200, Abcam, UK) and VEGF (1:300, Abcam, UK) were applied, and the sections were incubated overnight at 4°C. The following day, sections were incubated with HRP-conjugated secondary antibodies (1:500, Cell Signaling Technology, USA) for 1 hour, followed by DAB staining (Thermo Fisher Scientific, USA). Slides were counterstained with hematoxylin, sealed using neutral balsam, and subsequently examined and imaged under a light microscope.

Immunofluorescence (IF) Staining

IF staining was performed to observe the expression of HIF-1α and VEGF in tumor tissues. Tissue sections were incubated with primary antibodies against HIF-1α and VEGF (both from Abcam, USA). Following primary antibody incubation, sections were treated with fluorescently labeled secondary antibodies (Invitrogen, USA). DAPI (Thermo Fisher Scientific, USA) was used for counterstaining to visualize cell nuclei, providing a blue fluorescent contrast for cellular morphology. The stained sections were then examined using a confocal microscope (Leica Microsystems, Germany).

Flow Cytometry Detection of Apoptosis

To evaluate apoptosis in tumor-derived cells, tissues were enzymatically dissociated into single-cell suspensions and resuspended in binding buffer. Apoptosis levels were determined using an Annexin V-FITC/PI staining kit (BD Biosciences, USA). After staining, samples were immediately analyzed using a flow cytometer (BD FACSCanto II, BD Biosciences, USA). A minimum of 20,000 events were recorded per sample. Data were analyzed using FlowJo software (FlowJo, USA). All experiments were independently repeated three times to ensure reproducibility.

γ-H2AX Staining for DNA Damage Detection

DNA double-strand breaks (DSBs) were detected by immunofluorescence staining of γ-H2AX. Tumor tissue sections were incubated overnight at 4°C with an anti-γ-H2AX primary antibody (1:500, Cell Signaling Technology, USA), followed by a 1-hour incubation with an Alexa Fluor 488-conjugated secondary antibody (1:500, Invitrogen, USA). Nuclei were counterstained with DAPI (Thermo Fisher Scientific, USA). Imaging was conducted using a confocal microscope (Leica Microsystems, Germany), and signal quantification was performed with ImageJ software.

Data Analysis

All experiments were performed in triplicate, and the data are presented as mean ± standard deviation (SD). Statistical analyses were conducted using GraphPad Prism 9.0 (GraphPad Software, USA). Differences between groups were assessed using one-way analysis of variance (ANOVA), with p-values < 0.05 considered statistically significant.

Results

Successful Preparation of Peptide-Modified AuNPs Loaded with SAHA Complex

In this study, we successfully prepared RGD-AuNPs and loaded the HDAC inhibitor SAHA onto their surface, forming an RGD-AuNPs-SAHA complex (Figure 1A). First, AuNPs were synthesized using the citrate reduction method. A chloroauric acid solution (0.01 M) was heated to boiling at 100°C, followed by the rapid addition of 1% sodium citrate solution, with stirring for 15 minutes. The solution turned red, indicating the successful formation of AuNPs. DLS analysis revealed that the synthesized AuNPs possessed an average hydrodynamic diameter of approximately 20 nm and exhibited good dispersibility (Figure 1B).

Next, RGD peptides modified with thiol groups were conjugated to the surface of AuNPs using a thiol-gold binding method, resulting in RGD-AuNPs. During this process, a solution of thiol-modified RGD peptides (1 mM) was mixed with the AuNPs solution at a 10:1 volume ratio and stirred at ambient temperature for 12 hours. TEM images showed a slight increase in nanoparticle size after RGD peptide modification, while the nanoparticles maintained good dispersibility and spherical structure (Figure 1C). To further characterize the elemental chemical states of RGD-AuNPs, XPS and TEM combined with EELS mapping were employed. The XPS spectra and EELS loss peaks revealed that the RGD-AuNPs primarily consisted of C, N, O, and Au elements, all present in bound states (Figure 1D–E). These results confirm the successful synthesis of the RGD-modified AuNPs.

To quantify the number of RGD molecules bound to the surface of AuNPs, a deconvolution approach was used. The concentration of AuNPs was first determined using UV-Vis absorbance. This concentration was multiplied by Avogadro's number to calculate the total number of nanoparticles. The absorbance was then corrected to determine the concentration and absolute number of RGD molecules. Based on this analysis, 1.21 nM of AuNPs could be loaded with approximately 2.53×10^{17} RGD molecules (Figure 1F).

Subsequently, the HDAC inhibitor SAHA was loaded onto RGD-AuNPs via physical adsorption to form the RGD-AuNPs-SAHA complex. During this process, a SAHA solution (1 mM) was mixed with the RGD-AuNPs solution at a 1:10 ratio and stirred at ambient temperature for 6 hours. Unbound SAHA was removed through centrifugation and washing steps. UV-Vis and HPLC analyses confirmed an SAHA encapsulation rate of 85.2% and a loading efficiency of 75.6% (Figure 1G).

To further verify SAHA loading efficiency and nanoparticle stability, FTIR and TGA were employed for material characterization. The FTIR spectra show characteristic peaks for the RGD-AuNPs-SAHA complex at 3295 cm^{-1} and 1673 cm^{-1}, corresponding to the N-H stretching vibration in amide A and the C=O stretching vibration in amide I, respectively. The peak at 1563 cm^{-1} is attributed to the C-N stretching and N-H bending vibrations in amide II, while the peak at 777 cm^{-1} is associated with the out-of-plane bending vibration of N-H (Figure 1H). TGA analysis shows that the weight loss for the AuNPs group begins at a relatively low temperature (around 200°C), while the curves for the RGD-AuNPs and RGD-AuNPs-SAHA groups show significant weight loss only above 400°C, indicating that they have higher thermal stability. These results suggest that the modified AuNPs have greater thermal stability compared to the unmodified AuNPs (Figure 1I).

To evaluate the surface charge characteristics of the nanoparticles, a laser particle size analyzer was used to measure their zeta potential. The results showed that the zeta potential of AuNPs was −35 mV, which shifted to −25 mV after RGD peptide modification (RGD-AuNPs) and further to −20 mV following SAHA loading (RGD-AuNPs-SAHA) (Figure 1J). These results demonstrate that the nanoparticles retained structural stability during both surface modification and drug loading procedures.

Study on the Release and Stability of RGD-AuNPs-SAHA Under Different pH Conditions

We conducted in vitro drug release experiments under varying pH conditions (pH 7.4 and pH 5.5) to evaluate the release behavior of SAHA from RGD-AuNPs. The RGD-AuNPs-SAHA suspension was placed in a dialysis bag and incubated at 37°C in phosphate-buffered saline and acetate buffer to assess drug release. Samples were taken at regular intervals, and the concentration of released SAHA was measured using UV-Vis spectrophotometry to determine the release

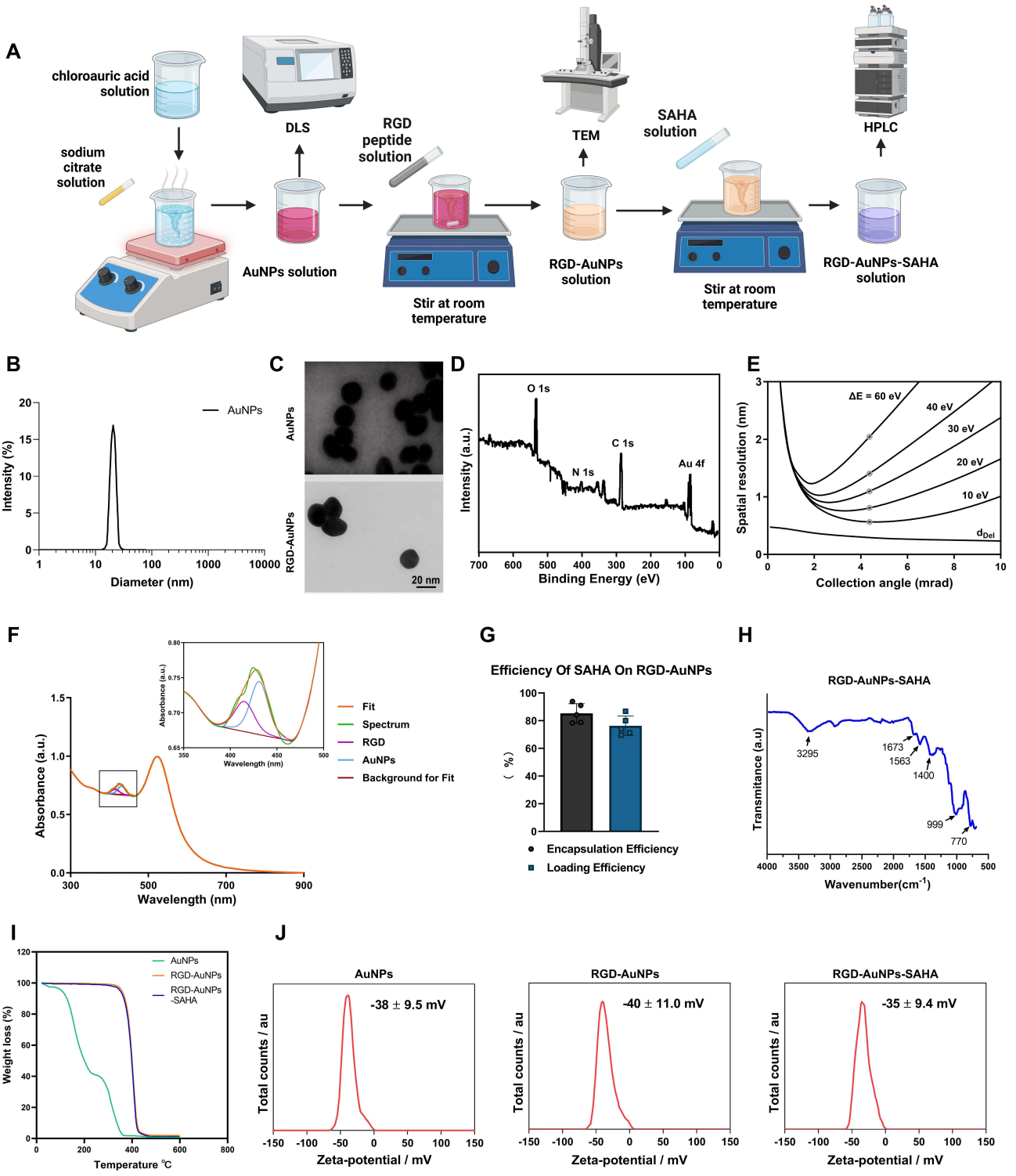

Figure 1 Preparation and Characterization of Peptide-Modified AuNPs Loaded with SAHA.

Note: (**A**) Synthesis of AuNPs via the citrate reduction method; (**B**) DLS analysis of AuNPs particle size distribution; (**C**) TEM observation of the morphology and size changes of RGD-AuNPs; (**D**) XPS was employed to analyze the elemental composition of RGD-AuNPs; (**E**) The chemical bonding states of elements were further characterized using TEM combined with EELS mapping; (**F**) The amount of RGD peptides on the surface of AuNPs was quantified using UV-Visible spectroscopy in conjunction with a Levenberg–Marquardt algorithm-based fitting approach. (**G**) Encapsulation efficiency and drug-loading capacity of SAHA measured by UV-Vis and HPLC; (**H**) FTIR analysis of characteristic absorption peaks of RGD-AuNPs-SAHA complexes; (**I**) TGA comparison of the thermal stability between RGD-AuNPs and RGD-AuNPs-SAHA; (**J**) Zeta potential measurements of nanoparticles at different stages using a laser particle size analyzer.

kinetics. The results indicated that at pH 5.5, the release rate of SAHA was significantly higher than at pH 7.4, with release rates of 60% and 35%, respectively, after 24 hours (Figure 2A).

To assess the stability of nanoparticles under physiological conditions, TEM and DLS were used to monitor changes in nanoparticle morphology and size under different conditions. RGD-AuNPs-SAHA solutions were incubated in buffer solutions at pH 7.4 and pH 5.5 at 37°C for 24 hours, with samples taken every 6 hours for characterization. TEM images revealed that the nanoparticles maintained a well-defined spherical structure under both pH conditions, with no significant aggregation observed (Figure 2B). DLS data showed that the particle size ranged from 20 nm to 25 nm at pH 7.4 and from 20 nm to 30 nm at pH 5.5, indicating a slight increase in size in the acidic environment (Figure 2C).

As shown in Figure 2D, the size and morphology of the nanoparticles were measured at various time points and under different pH conditions. The results indicate that the Zeta potential of RGD-AuNPs-SAHA nanoparticles remained relatively unchanged around −20 mV at both pH 7.4 and pH 5.5, suggesting that the surface charge of the nanoparticles remained stable across different pH environments.

The DLS results indicate that under pH 7.4 conditions, the average particle size of the nanoparticles showed minimal change between 7 and 14 days. At pH 5.5, the average particle sizes were 27 nm and 31 nm at 7 and 14 days, respectively. These findings suggest a slight increase in particle size under acidic conditions, consistent with the trend observed during the first 24 hours (Figure 2E).

TEM analysis revealed that the morphology of the nanoparticles was more regular and well-dispersed at pH 7.4. In contrast, under pH 5.5, some nanoparticles exhibited aggregation and slight morphological changes, though their overall structure remained stable (Figure 2F).

Peptide-Modified AuNPs Conjugated with SAHA Exhibit Good Biocompatibility and Low Toxicity

The biocompatibility of RGD-AuNPs-SAHA was assessed in normal alveolar epithelial cells (TT1) using the MTT assay. Cells were exposed to 50 μM concentrations of AuNPs, SAHA, RGD-AuNPs, or RGD-AuNPs-SAHA for 24 and 48 hours, with untreated cells serving as controls. After 24 hours, the cell viability in the AuNPs group was 97%, while the RGD-AuNPs, SAHA, and RGD-AuNPs-SAHA groups exhibited a cell viability of approximately 95% (Figure 3A).

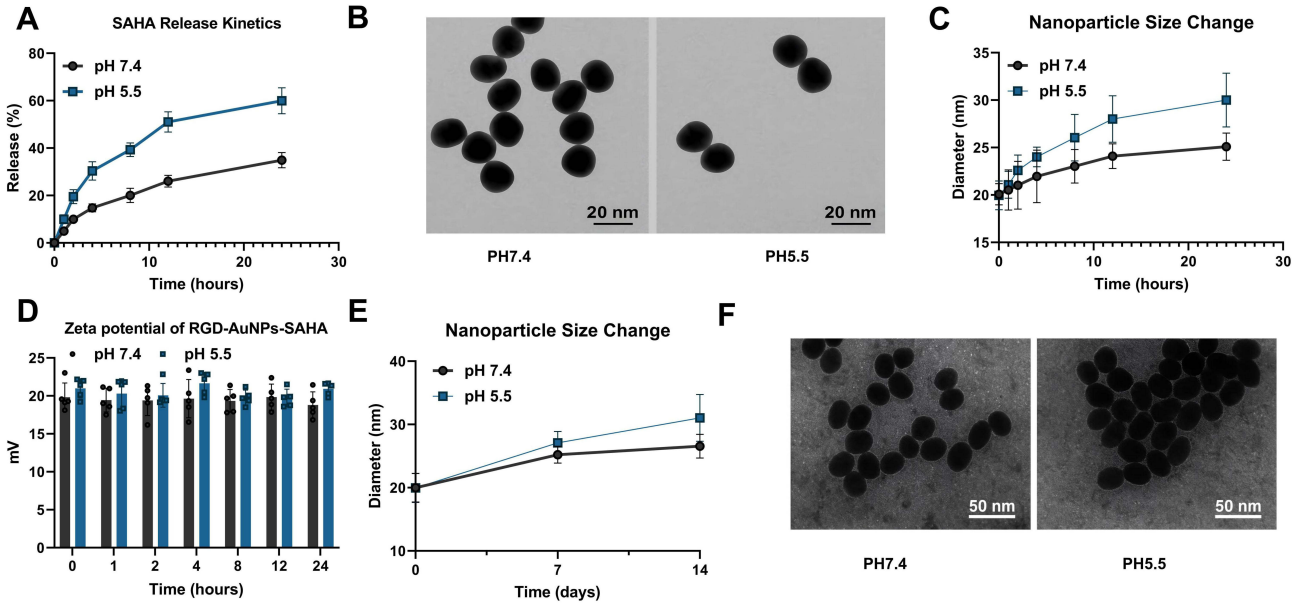

Figure 2 Release Behavior and Stability of RGD-AuNPs-SAHA under Different pH Conditions.
Note: (**A**) Comparison of SAHA release rates at pH 7.4 and pH 5.5; (**B**) TEM images showing nanoparticle structures under different pH conditions, scale bar = 20 nm; (**C**) DLS data illustrating particle size changes at pH 7.4 and pH 5.5; (**D**) Zeta potential measurements of nanoparticles at pH 7.4 and pH 5.5 using a laser particle size analyzer; (**E** and **F**) Nanoparticle size and morphology changes after 7 and 14 days of incubation at pH 7.4 and pH 5.5, as measured by DLS and TEM, scale bar = 50 nm.

https://doi.org/10.2147/IJN.S531731

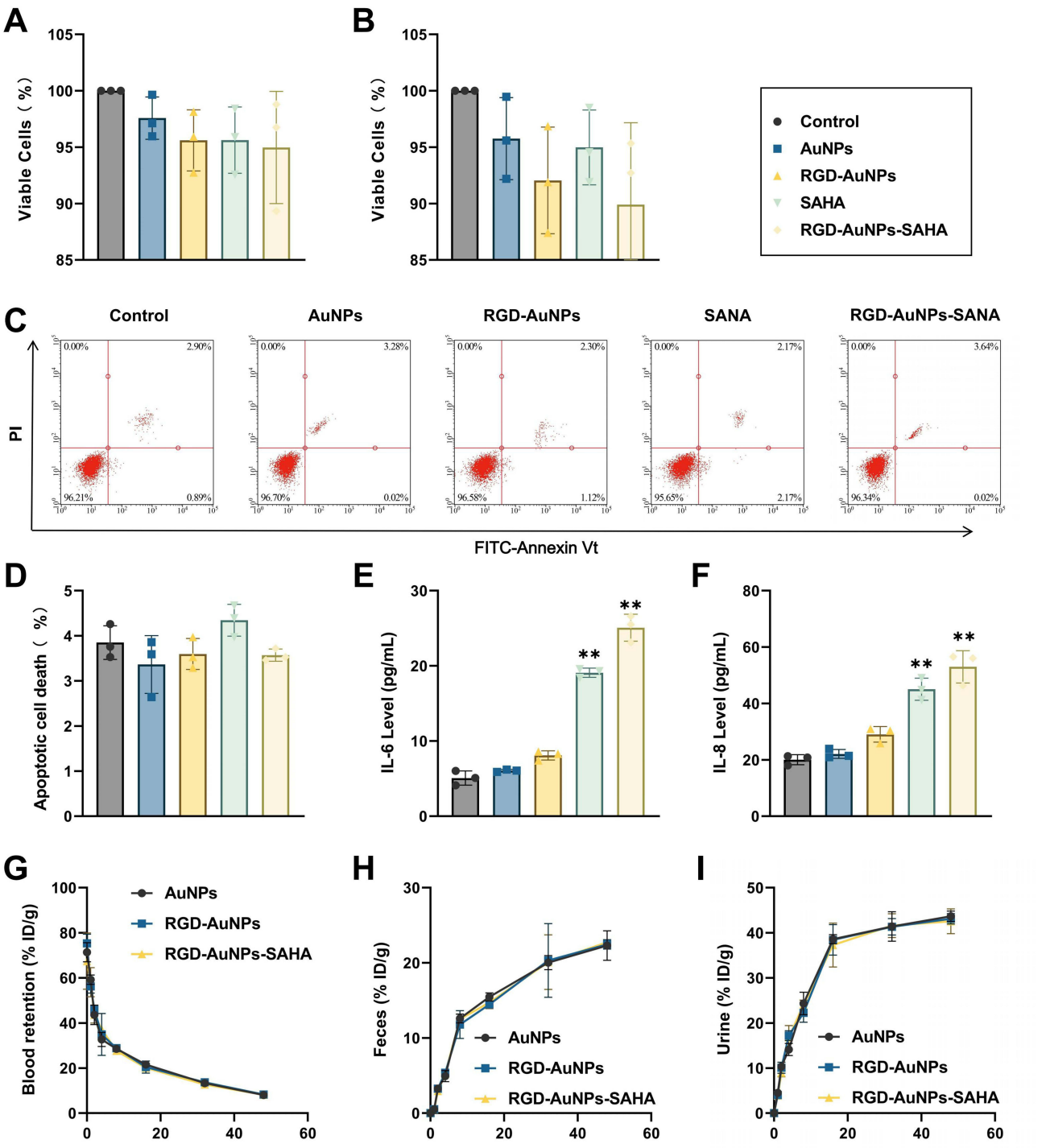

Figure 3 Toxicity and Inflammatory Response of Normal Cells After RGD-AuNPs-SAHA Treatment.

Note: (**A**) Cell viability of TT1 cells after 24 hours of treatment, as measured by the MTT proliferation assay; (**B**) Cell viability of TT1 cells after 48 hours of treatment, as measured by the MTT proliferation assay; (**C**) Apoptosis analysis of TT1 cells following different treatments, based on flow cytometry; (**D**) Quantitative analysis of apoptosis in TT1 cells following different treatments, based on flow cytometry; (**E**) IL-6 levels in the culture supernatant of each group, measured by ELISA; (**F**) IL-8 levels in the culture supernatant of each group, measured by ELISA; (**G**) Plasma concentration of AuNPs over time following intravenous injection; (**H**) Cumulative excretion of AuNPs in feces at different time points; (**I**) Cumulative excretion of AuNPs in urine at different time points. Each experiment was repeated three times (n=3). $^{**}p < 0.01$.

After 48 hours, the cell viability in the RGD-AuNPs and RGD-AuNPs-SAHA groups decreased to around 90%, although this reduction was not different from the control group (Figure 3B). These results suggest that while RGD-AuNPs-SAHA exhibits mild cytotoxicity towards normal cells, the effect is minimal, and the toxicity remains very low.

To further investigate potential apoptotic effects, Annexin V-FITC/PI dual staining followed by flow cytometry was conducted. Cells were categorized into live, early apoptotic, late apoptotic, and necrotic populations (Figure 3C). Quantitative analysis showed no significant differences in necrosis rates among the groups (Figure 3D). These results suggest that RGD-AuNPs-SAHA has no impact on necrosis in normal cells.

In addition, we used ELISA to measure the levels of inflammatory cytokines IL-6 (Figure 3E) and IL-8 (Figure 3F) in the culture supernatant of each group. No significant elevation in cytokine levels was observed in the blank nanoparticle group compared to the control. In contrast, mild but statistically significant increases in IL-6 and IL-8 were detected in the SAHA and RGD-AuNPs-SAHA groups, indicating a modest inflammatory response without evidence of overt immunotoxicity.

To assess the biocompatibility, pharmacokinetic properties, and excretion pathways of AuNPs in vivo, we administered different nanoparticle formulations to normal mice via tail vein injection. Blood and major organs were periodically collected for histopathological examination and biochemical analysis. Additionally, blood, urine, and feces were collected at various time points, and gold concentrations were measured using ICP-MS. The time-dependent blood circulation curves of the different groups of AuNPs indicated a blood clearance half-life of 2 to 3 hours (Figure 3G). The time-dependent accumulation of ultra-small AuNPs in feces (Figure 3H) and urine (Figure 3I) suggested that renal clearance, rather than intestinal excretion, was the primary route of elimination for these particles.

Additionally, histopathological examination revealed that the heart, liver, spleen, kidney, and lung tissues of mice in the different treatment groups exhibited intact structures with no significant pathological changes (Figure S1A). ELISA results showed no significant differences in blood levels of tumor necrosis factor TNF-α (Figure S1B) and interleukin IL-6 (Figure S1C) between groups, indicating that the AuNPs used at the experimental concentrations did not trigger a noticeable immune response. There were also no significant differences between groups in liver function markers, including AST (Figure S1D) and ALT (Figure S1E), or in kidney function markers, such as CREA (Figure S1F) and BUN (Figure S1G). Additional biochemical parameters remained within normal physiological ranges and showed no notable deviations among groups (Table 1).

The results indicate that RGD-AuNPs-SAHA exhibits minimal toxicity and a mild inflammatory response in normal cells in vitro. In vivo, RGD-AuNPs-SAHA showed no significant impact on key biochemical markers or organ structure in mice, demonstrating excellent biocompatibility and negligible toxicity. These findings provide crucial theoretical support and experimental data for the further study and development of this nanomaterial in cancer therapy.

Polypeptide-Modified AuNPs Loaded with SAHA Significantly Inhibit NSCLC Cell Proliferation

To determine whether polypeptide-modified AuNPs loaded with SAHA exert direct cytotoxic effects on human lung cancer cells, this study treated human NSCLC cell lines A549 and Calu-1 with AuNPs, SAHA, RGD-AuNPs, and RGD-AuNPs-SAHA. The effects on cell growth and apoptosis were evaluated, and the experimental workflow is illustrated in Figure 4A.

Cell viability was first assessed using the CCK-8 assay (Figure 4B and C). Both SAHA and RGD-AuNPs-SAHA treatments significantly reduced proliferation compared to controls. Notably, the RGD-AuNPs-SAHA group exhibited the most pronounced inhibition, with proliferation rates reduced by 55% in Calu-1 cells (Figure 4B) and 49% in A549 cells (Figure 4C).

To further confirm the antiproliferative effect of RGD-AuNPs-SAHA, clonogenic assays were conducted in Calu-1 and A549 cell lines (Figure 4D–F). Treatment with RGD-AuNPs-SAHA resulted in a marked decrease in colony formation compared to other groups, indicating a significant impairment in long-term proliferative and survival capacity. These results provide strong evidence that RGD-AuNPs-SAHA effectively suppresses the clonogenic potential of NSCLC cells.

The impact on tumor cell motility was further investigated using wound healing and Transwell assays (Figure 4G–J). Scratch wound healing assays revealed that cells in the RGD-AuNPs-SAHA group migrated significantly shorter distances compared to other groups. Specifically, Calu-1 cells exhibited a wound healing rate of less than 50% within

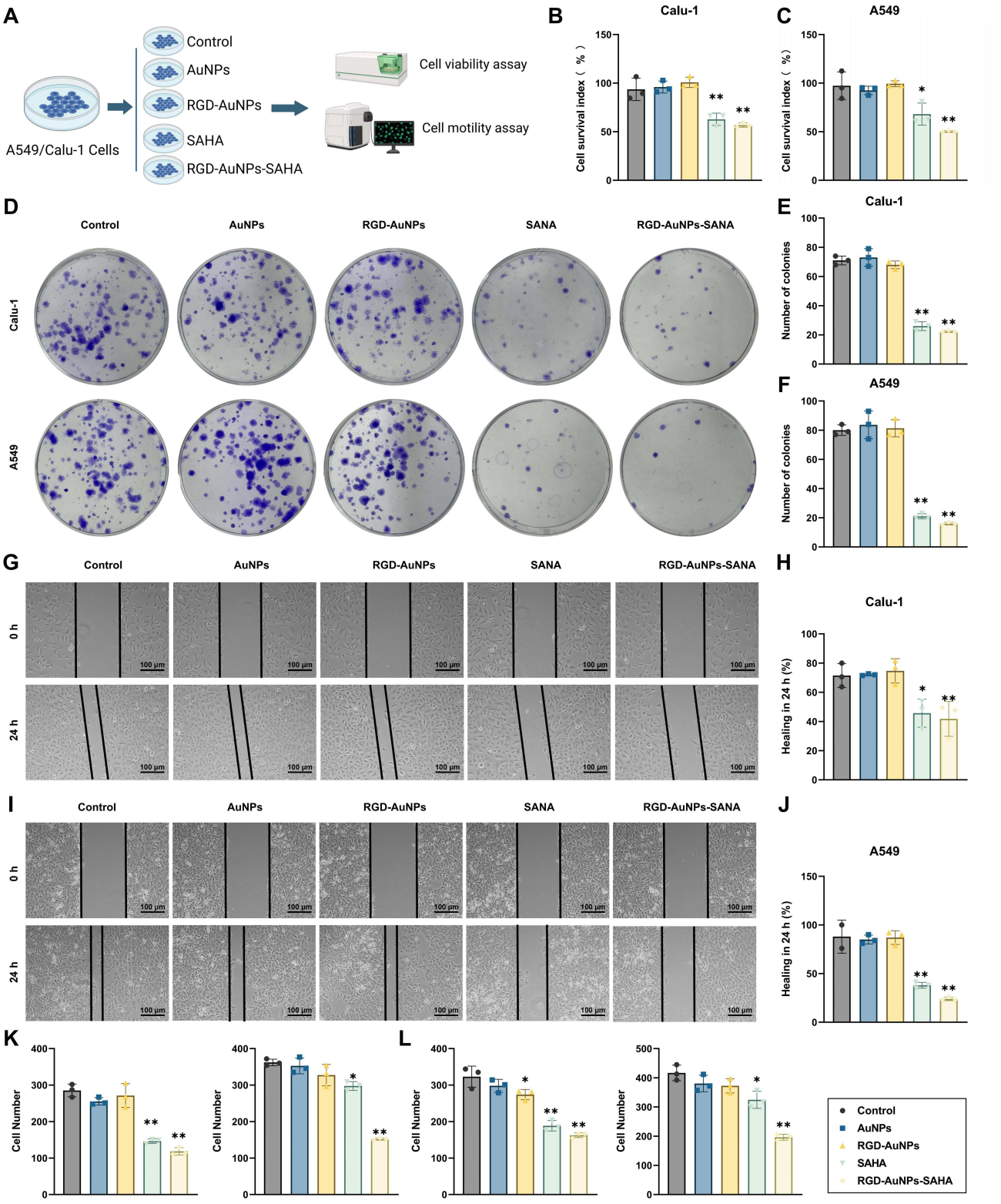

Figure 4 Effects of RGD-AuNPs-SAHA Treatment on the Proliferation, Migration, and Invasion of Human NSCLC Cells.

Note: (**A**) Experimental workflow for the effects of RGD-AuNPs-SAHA treatment on cell proliferation, apoptosis, migration, and invasion; (**B**) CCK-8 assay measuring Calu-1 cell viability; (**C**) CCK-8 assay measuring A549 cell viability across different groups; (**D**) Representative images from colony formation assays; (**E**) Quantification of colony numbers in Calu-1 cells; (**F**) Quantification of colony numbers in A549 cells; (**G**) Representative images of scratch assays assessing the migration ability of Calu-1 cells; (**H**) Statistical analysis of 24-hour migration ability of Calu-1 cells across groups in the scratch assay; (**I**) Representative images of scratch assays assessing the migration ability of A549 cells; (**J**) Statistical analysis of 24-hour migration ability of A549 cells across groups in the scratch assay; (**K**) Transwell invasion assay assessing the invasion ability of Calu-1 cells across groups; (**L**) Transwell invasion assay assessing the invasion ability of A549 cells across groups. Unless otherwise specified, each experiment was performed in triplicate (n=3). *$p < 0.05$, **$p < 0.01$.

24 hours, while A549 cells had a wound healing rate of less than 40%, both of which were significantly lower than the 70% healing rates observed in the control and AuNP-only groups. This indicates that RGD-AuNPs-SAHA markedly inhibits the migration ability of A549 cells. Additionally, Transwell migration and invasion assays were conducted to further evaluate the effect on cell motility (Figure 4K and L). The results showed that both the RGD-AuNPs-SAHA and SAHA groups had a significantly lower number of invasive cells compared to other groups. Moreover, the RGD-AuNPs-SAHA group exhibited a significantly reduced number of migrating cells compared to the other groups. These findings suggest that RGD-AuNPs-SAHA effectively suppresses the motility of both Calu-1 and A549 cells.

Collectively, these results demonstrate that polypeptide-modified AuNPs enhance the targeting efficacy of SAHA, significantly inhibiting proliferation, migration, and invasion in human NSCLC cell lines A549 and Calu-1. These findings provide a crucial theoretical foundation and experimental support for further research into their potential applications in cancer therapy.

Polypeptide-Modified AuNPs Loaded with SAHA Induce Apoptosis in Small Cell Lung Cancer Cells

HDACs are crucial components of the epigenetic mechanisms regulating gene expression and are implicated as oncogenes in various cancer types.[31] SAHA, an HDAC inhibitor, directly elevates acetylated histone levels by inhibiting HDAC activity.

To evaluate the inhibitory effect of SAHA (either alone or in combination with AuNPs) on HDAC enzymes, this study utilized A549 and Calu-1 cells. These cells were exposed to 6.8 μM AuNPs, 0.1 μM SAHA, or a combination of both (Figure 5A). Acetylated lysine levels within the cells were observed using fluorescence microscopy and quantified with an ELISA. Cells exposed to SAHA alone or in combination with AuNPs exhibited significantly elevated acetylation levels compared to the control and AuNP-only groups (Figure 5B–E). Thus, it can be concluded that SAHA effectively inhibits HDAC activity when used in conjunction with AuNPs, with no evidence of antagonistic interactions between the two agents.

Additionally, to investigate the effects of polypeptide-modified AuNPs loaded with SAHA on apoptosis in NSCLC cells, we assessed nuclear morphology using Hoechst staining. The results indicated that both the SAHA and RGD-AuNPs-SAHA groups significantly induced the formation of apoptotic bodies in Calu-1 and A549 cells (Figure 5F; Figure 5H), with no significant differences in apoptosis observed in the control, AuNPs, and RGD-AuNPs groups. Notably, the RGD-AuNPs-SAHA group exhibited the highest apoptosis rate (Figure 5G; Figure 5H), demonstrating the most effective cancer cell killing. Flow cytometry further confirmed that both the SAHA and RGD-AuNPs-SAHA groups induced significant apoptosis compared to the control group, with the RGD-AuNPs-SAHA group showing the highest proportion of apoptotic cells (Figure 5I–K). These findings suggest that RGD-AuNPs-SAHA effectively inhibits proliferation and promotes apoptosis in human lung cancer cells in vitro.

The above research indicates that SAHA effectively inhibits HDAC, leading to a significant increase in acetylation levels within cells, thereby promoting tumor cell apoptosis. Notably, the combination of SAHA with RGD-AuNPs enhances this effect, resulting in a marked increase in the proportion of apoptotic cells.

Based on these findings, it can be concluded that polypeptide-modified AuNPs loaded with SAHA, through their unique supramolecular self-assembly, improve drug delivery efficiency and enhance drug accumulation at tumor sites. This approach effectively activates apoptotic pathways and provides a novel targeted drug delivery system for lung cancer therapy.

Polypeptide-Modified AuNPs Loaded with SAHA Regulate Hypoxic Microenvironment and Inhibit Lung Cancer Cells

Hypoxia is a common feature of solid tumors and can activate angiogenesis, increase invasiveness and metastatic risk, enhance tumor survival, and suppress antitumor immune responses, thereby diminishing therapeutic efficacy.[32–34]

In this study, the expression of hypoxia-related genes and proteins in A549 cells was assessed using RT-qPCR and ELISA. The results indicated that the levels of hypoxia-regulated cytoplasmic proteins HIF-1α and VEGF were lower in

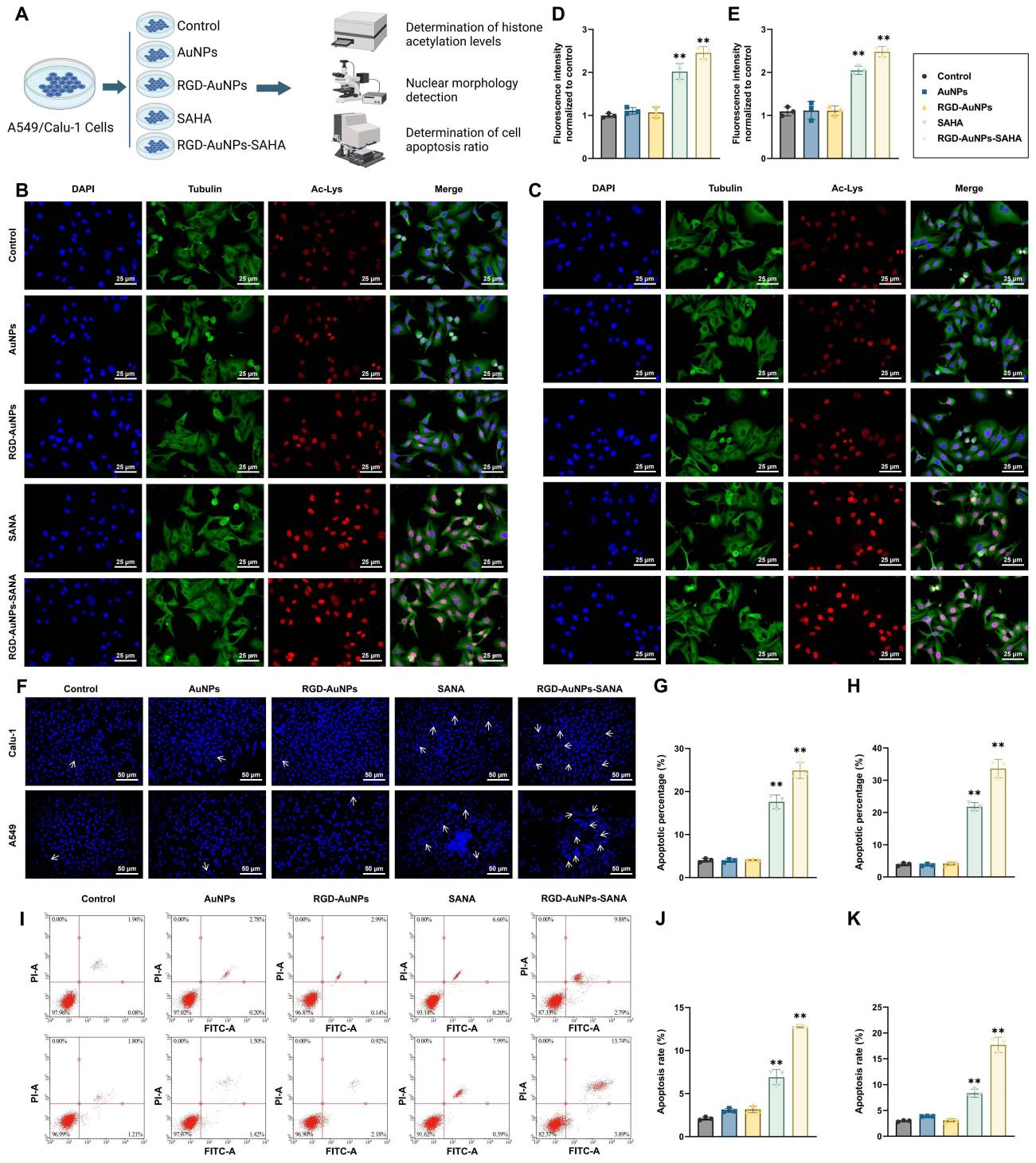

Figure 5 Effect of RGD-AuNPs-SAHA Treatment on Apoptosis in Human NSCLC Cells.

Note: (**A**) Schematic of the experimental process showing the effect of RGD-AuNPs-SAHA on HDAC activity and cell apoptosis; (**B**) Fluorescence microscopy detecting acetylated lysine levels in Calu-1 cells; (**C**) Fluorescence microscopy detecting acetylated lysine levels in A549 cells; (**D**) Quantification of acetylated lysine levels in Calu-1 cells by microplate reader; (**E**) Quantification of acetylated lysine levels in A549 cells by microplate reader; (**F**) Representative images of nuclear morphology in lung cancer cells under different treatments using Hoechst 33258 staining, with apoptotic bodies indicated by white arrows; (**G**) Hoechst 33258 staining of nuclear morphology in Calu-1 cells under different treatments; (**H**) Hoechst 33258 staining of nuclear morphology in A549 cells under different treatments; (**I**) Representative images of apoptosis in Calu-1 and A549 cells after 24 hours of treatment, detected by flow cytometry using Annexin V-FITC and PI staining; (**J**) Flow cytometric analysis of apoptosis rates in Calu-1 cells; (**K**) Flow cytometric analysis of apoptosis rates in A549 cells. Each experiment was repeated three times (n=3) unless otherwise stated. $^{**}p < 0.01$.

the SAHA, RGD-AuNPs, and RGD-AuNPs-SAHA groups compared to the control and AuNP-only groups. Notably, the RGD-AuNPs-SAHA group demonstrated the most pronounced inhibition, with mRNA levels of HIF-1α and VEGF decreasing (Figure 6B and C). ELISA results further confirmed a substantial reduction in the corresponding protein levels (Figure 6D and E). These findings suggest that RGD-AuNPs-SAHA effectively regulates the hypoxic microenvironment in tumor cells.

The JAK2/STAT3 signaling pathway plays a crucial role in tumorigenesis and angiogenesis, with VEGF acting as a downstream target gene of JAK2/STAT3. Western blot analysis of protein expression levels (Figure 6F and G) revealed that SAHA inhibits the activation of this pathway relative to the control group, with the most pronounced inhibition found in the RGD-AuNPs-SAHA group. This inhibition effectively prevents angiogenesis and consequently suppresses tumor growth. Butyzamide was found to increase the phosphorylation levels of JAK2 and STAT3, and rescue experiments further confirmed that RGD-AuNPs-SAHA inhibits the JAK2/STAT3 signaling pathway, thereby obstructing angiogenesis and suppressing tumor growth.

Excessive ROS can induce oxidative stress, leading to cell death. Quantitative assessment of intracellular ROS levels revealed a significant elevation in the RGD-AuNPs-SAHA group, with ROS levels approximately twofold higher than those observed in the control group (Figure 6H). This indicates that RGD-AuNPs-SAHA treatment markedly enhances oxidative stress in A549 cells, providing further evidence of its antitumor mechanism.

Flow cytometric analysis was conducted to examine cell cycle distribution following treatment. Compared with the untreated control, RGD-AuNPs-SAHA treatment significantly increased the proportion of cells in the G1 phase while reducing the percentages of cells in the S and G2/M phases, suggesting that it inhibits cell proliferation by inducing G1 phase arrest (Figure S2A and B). Subsequently, Western blot analysis was performed to assess the expression of key cell cycle regulatory proteins (Figure S2C). The results demonstrated an upregulation of the cyclin-dependent kinase inhibitors p21 and p27, alongside downregulation of p-AKT, CDK1/2, and cyclin B, further supporting G1 phase arrest (Figure S2D).

Finally, a rescue experiment was designed to evaluate the impact of HIF-1α overexpression on the effects of RGD-AuNPs-SAHA treatment in A549 cells. The results of the scratch assay revealed that the HIF-1α overexpression group had the highest healing rate, indicating that HIF-1α overexpression significantly mitigated the effects of RGD-AuNPs-SAHA on cell proliferation (Figure S2E).

Hoechst staining results indicated no significant difference in apoptosis rates between the HIF-1α overexpression group and the control group. HIF-1α overexpression was found to attenuate the cytotoxic effect of RGD-AuNPs-SAHA on A549 cells (Figure S2F), a finding consistent with flow cytometry results (Figure S2G). This suggests that RGD-AuNPs-SAHA exerts its antitumor effects through the inhibition of the HIF-1α pathway.

Collectively, these findings suggest that RGD-AuNPs-SAHA enhances histone acetylation in A549 cells and regulates the expression of cell cycle-related proteins, including downregulation of Cyclin B and CDK1/2, thereby inducing cell cycle arrest. Additionally, these nanoparticles significantly modulate the hypoxic microenvironment, enhance oxidative stress responses, suppress cell proliferation, and induce apoptosis via the HIF-1α pathway (Figure 6A). These findings provide a crucial theoretical foundation and experimental support for further research into their potential applications in cancer therapy.

Fluorescence Labeling Reveals the Uptake and Distribution of RGD-AuNPs-SAHA in NSCLC

In this study, FITC labeling was used to track RGD-AuNPs-SAHA, and confocal microscopy was employed to observe the nanoparticles' cellular uptake and localization at different time points (1 hour, 2 hours, and 4 hours). A549 NSCLC cells were selected as the experimental model and divided into five groups: control, unloaded nanoparticles, SAHA, RGD-AuNPs, and RGD-AuNPs-SAHA. Fluorescence intensity in the RGD-AuNPs and RGD-AuNPs-SAHA groups increased over time, with similar fluorescence levels observed in both groups. In contrast, the control, unloaded nanoparticles, and SAHA groups showed minimal internalization (Figure 7A). This suggests that polypeptide-modified AuNPs enhance cellular uptake. As there was no fluorescence signal in the unloaded nanoparticles and SAHA groups,

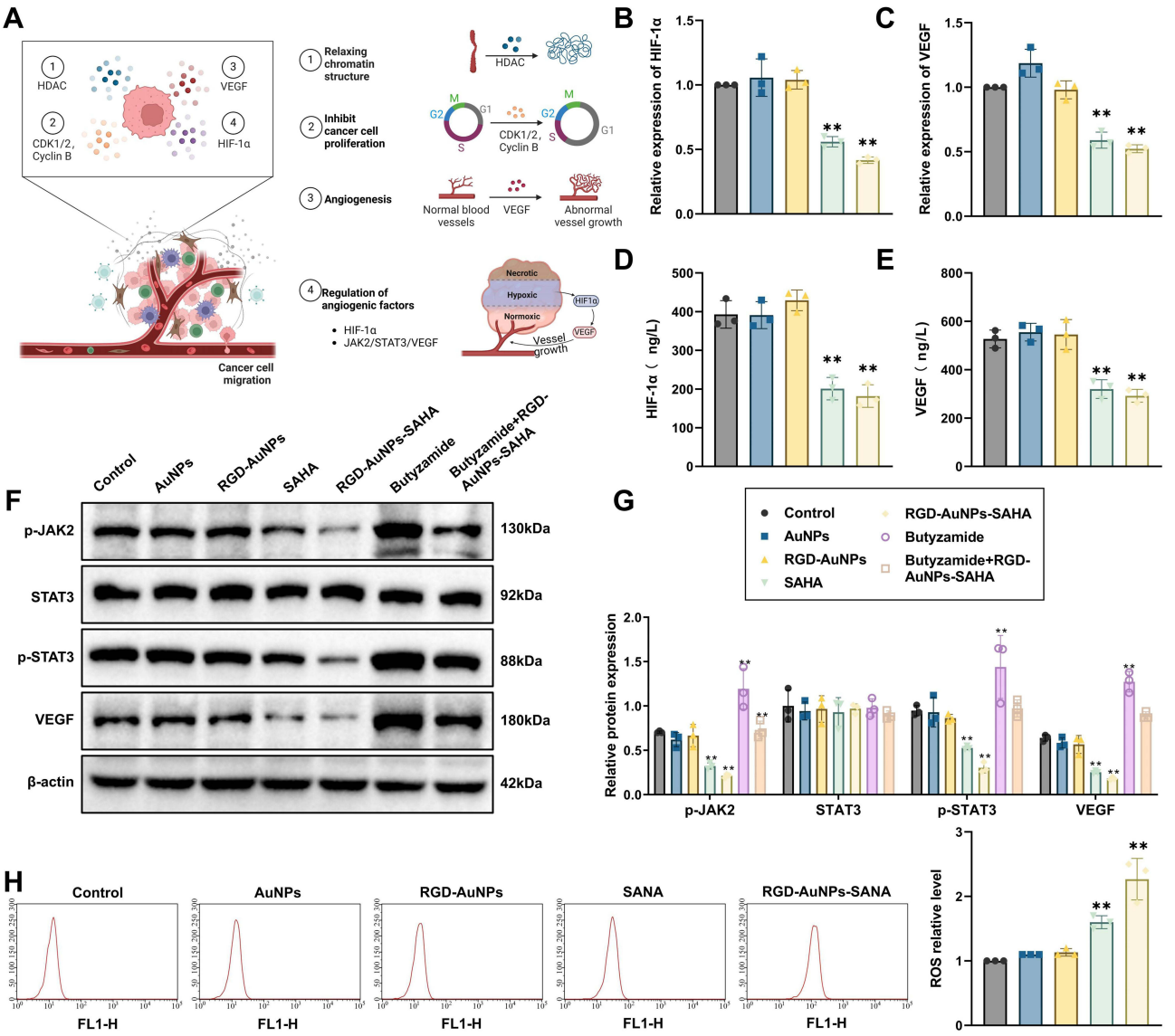

Figure 6 Polypeptide-Modified AuNPs with SAHA Regulate the Hypoxic Microenvironment to Inhibit Lung Cancer Cells.
Note: (**A**) Schematic illustration of the mechanism by which polypeptide-modified AuNPs with SAHA regulate the hypoxic microenvironment; (**B**) RT-qPCR analysis of HIF-1α mRNA expression levels in A549 cells across different groups; (**C**) RT-qPCR analysis of VEGF mRNA expression levels in A549 cells across different groups; (**D**) ELISA analysis of HIF-1α protein expression levels in A549 cells across different groups; (**E**) ELISA analysis of VEGF protein expression levels in A549 cells across different groups; (**F**) Western blot analysis of p-JAK2, STAT3, p-STAT3, VEGF, and the internal control β-actin; (**G**) Quantitative analysis of p-JAK2, STAT3, p-STAT3, and VEGF protein levels; (**H**) Flow cytometry analysis of ROS accumulation; ** indicates $p < 0.01$.

LysoTracker staining was performed on the control, RGD-AuNPs, and RGD-AuNPs-SAHA groups. LysoTracker staining revealed that the green fluorescence of RGD-AuNPs-SAHA highly co-localized with the red fluorescence of LysoTracker, indicating that these nanoparticles are primarily taken up by lysosomes (Figure 7B). The increased fluorescence intensity suggests that RGD-AuNPs and RGD-AuNPs-SAHA treatment may enhance lysosomal activity or lead to degradation of the nanoparticles within lysosomes.

Flow cytometry analysis demonstrated that the RGD-AuNPs-SAHA group exhibited the highest fluorescence intensity at all time points, significantly surpassing the control, AuNP-only, and SAHA groups. This indicates that cells have the greatest uptake efficiency for RGD-modified SAHA-loaded nanoparticles. Specifically, fluorescence intensity for the RGD-AuNPs-SAHA group was markedly higher at 1 hour, 2 hours, and 4 hours. In contrast, the fluorescence intensity in the control group remained nearly unchanged. The AuNP-only and SAHA groups showed lower fluorescence intensities of 10.48 AU and 6.37 AU, respectively, indicating lower nanoparticle and drug uptake efficiency.

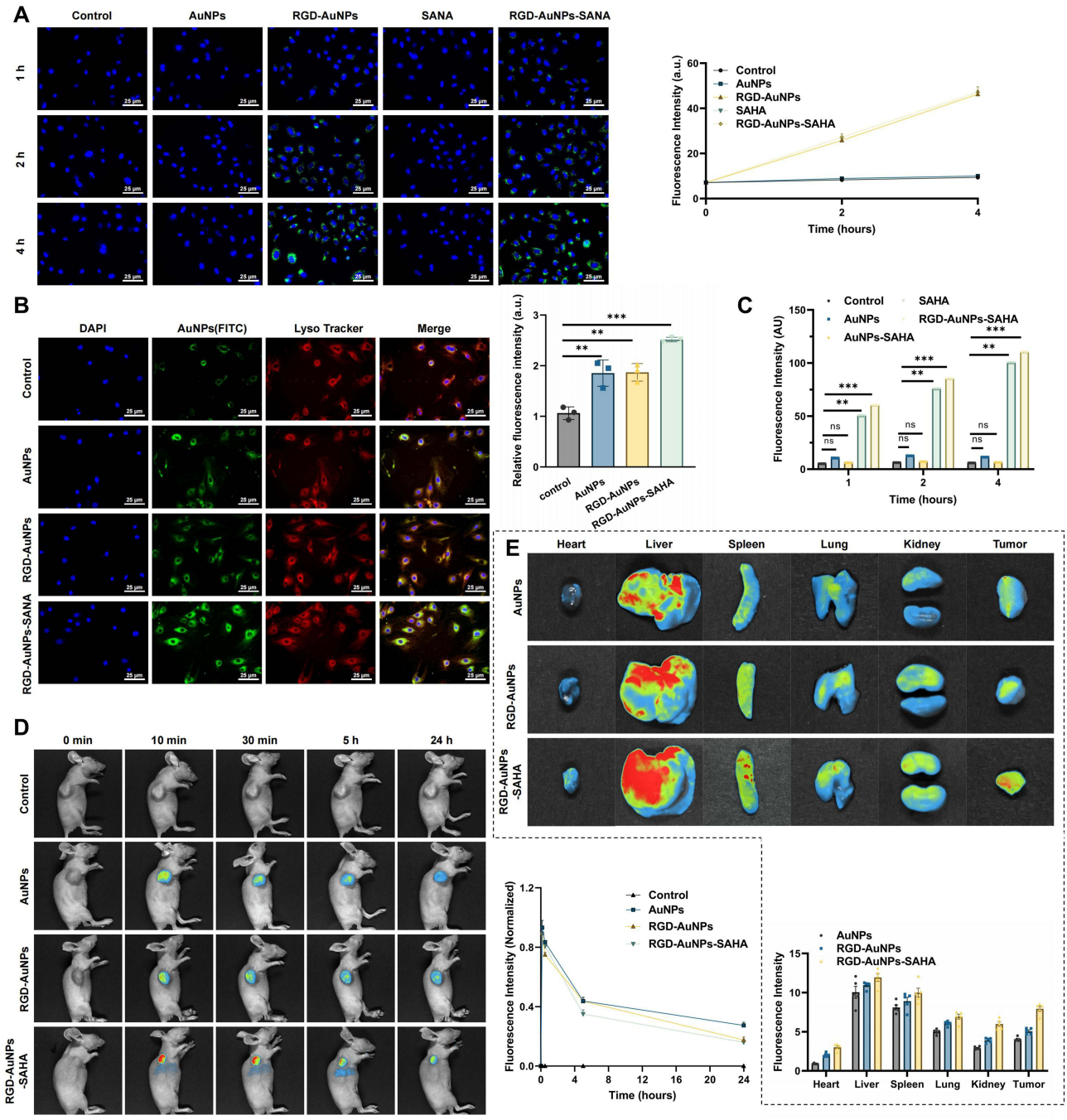

Figure 7 Cellular Uptake and In Vivo Distribution of RGD-AuNPs-SAHA.

Note: (**A**) Confocal microscopy showing the uptake and distribution of nanoparticles in A549 cells at different time points (1 hour, 2 hours, and 4 hours), with a scale bar of 25 μm; (**B**) Colocalization of FITC and LysoTracker in each group; (**C**) Flow cytometry quantification of fluorescence intensity in each group (Control, AuNPs, RGD-AuNPs, SAHA, and RGD-AuNPs-SAHA), n=5; (**D**) In vivo biodistribution of fluorescently labeled nanoparticles and their complexes after intravenous injection in mice, observed through a live imaging system; (**E**) Major sites of nanoparticle distribution. ns indicates $p > 0.05$, $^{**}p < 0.01$, $^{***}p < 0.001$.

Over time, the fluorescence intensity in both RGD-AuNPs and RGD-AuNPs-SAHA groups increased significantly, with the RGD-AuNPs-SAHA group demonstrating the highest fluorescence intensity, reflecting the most effective nanoparticle uptake (Figure 7C).

In the in vivo experiments, fluorescently labeled AuNPs were administered via tail vein injection, and their biodistribution in mice was monitored using an in vivo imaging system (Figure 7D). The results indicated that the nanoparticles predominantly accumulated in the liver, spleen, and lungs. Over time, the fluorescence signal intensity

https://doi.org/10.2147/IJN.S531731

diminished throughout the body. Notably, fluorescence signals persisted even 24 hours post-injection (Figure 7E). These findings suggest that RGD-AuNPs-SAHA exhibits favorable distribution and retention properties in vivo, highlighting its potential for significant therapeutic application in NSCLC.

RGD-AuNPs-SAHA Significantly Inhibits Tumor Growth and Improves the Inflammatory Microenvironment

In in vivo animal experiments, we treated A549 cell xenograft mouse models with the drug (Figure 8A) and regularly measured tumor volume and body weight while monitoring changes in the tumor hypoxic microenvironment. The results demonstrated that treatment with RGD-AuNPs-SAHA led to a marked reduction in tumor growth compared to the control group (Figure 8B). Specifically, by day 14 of treatment, the tumor volume in the RGD-AuNPs-SAHA group decreased by approximately 60% (Figure 8C). Furthermore, while the SAHA and RGD-AuNPs groups also showed some reduction in tumor volume, their effects were less pronounced than those observed with RGD-AuNPs-SAHA. Weight measurements of the tumor-bearing mice over 14 days revealed that the control and AuNP-only groups showed slow weight gain, whereas the SAHA group demonstrated a more rapid increase in body weight, with the RGD-AuNPs-SAHA group showing the most significant weight gain (Figure 8D). These findings suggest that the combined treatment not only effectively inhibited tumor growth but also significantly enhanced weight gain, potentially indicating improved health or reduced tumor burden in the treated mice.

We evaluated the impact of RGD-AuNPs-SAHA on inflammation in mice by measuring various cytokine levels in the serum. The results demonstrated that the levels of pro-inflammatory cytokines, such as TNF-α and IL-6, were lower in the RGD-AuNPs-SAHA group compared to the control, empty nanoparticle, SAHA, and RGD-AuNPs groups (Figure 8E and F). In contrast, levels of the anti-inflammatory cytokine IL-10 were markedly elevated in the RGD-AuNPs-SAHA group relative to all other treatment groups (Figure 8G). Notably, on day 14, TNF-α and IL-6 levels were reduced by a greater magnitude in the RGD-AuNPs-SAHA group than in the SAHA and RGD-AuNPs groups, which exhibited only modest reductions compared to the control. Concurrently, IL-10 concentrations were significantly upregulated in the RGD-AuNPs-SAHA group, further corroborating its immunomodulatory potential. These data indicate that RGD-AuNPs -SAHA not only suppresses pro-inflammatory responses but also promotes anti-inflammatory signaling, suggesting its therapeutic promise in mitigating inflammation-associated tumor progression.

RGD-AuNPs-SAHA Improves Tumor Microenvironment by Reducing Oxidative Stress

We assessed the impact of RGD-AuNPs-SAHA on oxidative stress levels in mice by measuring serum levels of SOD, CAT, and MDA. The results revealed that the SOD levels in the RGD-AuNPs-SAHA group were significantly higher than those in the control, AuNP-only, SAHA, and RGD-AuNPs groups (Figure 9A). This indicates that RGD-AuNPs-SAHA substantially increases SOD levels, thereby enhancing antioxidant capacity. Similarly, CAT levels in the RGD-AuNPs-SAHA group were significantly higher compared to other groups (Figure 9B), suggesting that RGD-AuNPs-SAHA markedly improves CAT levels and enhances hydrogen peroxide clearance. Additionally, MDA levels in the RGD-AuNPs-SAHA group were significantly lower than those in the control, AuNP-only, SAHA, and RGD-AuNPs groups (Figure 9C). This finding demonstrates that RGD-AuNPs-SAHA effectively reduces lipid peroxidation and minimizes oxidative stress damage.

Flow cytometry was used to assess the infiltration of immune cells (such as $CD8^+$ T cells, M1 and M2 macrophages) in tumor tissue to evaluate the impact of RGD-AuNPs-SAHA on the tumor immune microenvironment. The results indicated that the RGD-AuNPs-SAHA group exhibited significantly greater immune cell infiltration compared to the control, AuNP-only, SAHA, and RGD-AuNPs groups. Specifically, the number of $CD8^+$ T cells and M1 macrophages was significantly increased (Figure 9D and E), while the number of M2 macrophages was notably decreased (Figure 9F), suggesting a pronounced enhancement in tumor immune response.

Full blood cell counts were analyzed to evaluate the quantities and morphology of red blood cells, white blood cells, and platelets in the blood samples from the mice (Figure 9G–I). The results showed that all cell types were within normal ranges. In the AuNP-only group, there was a slight increase in cell counts, but the differences compared to the control

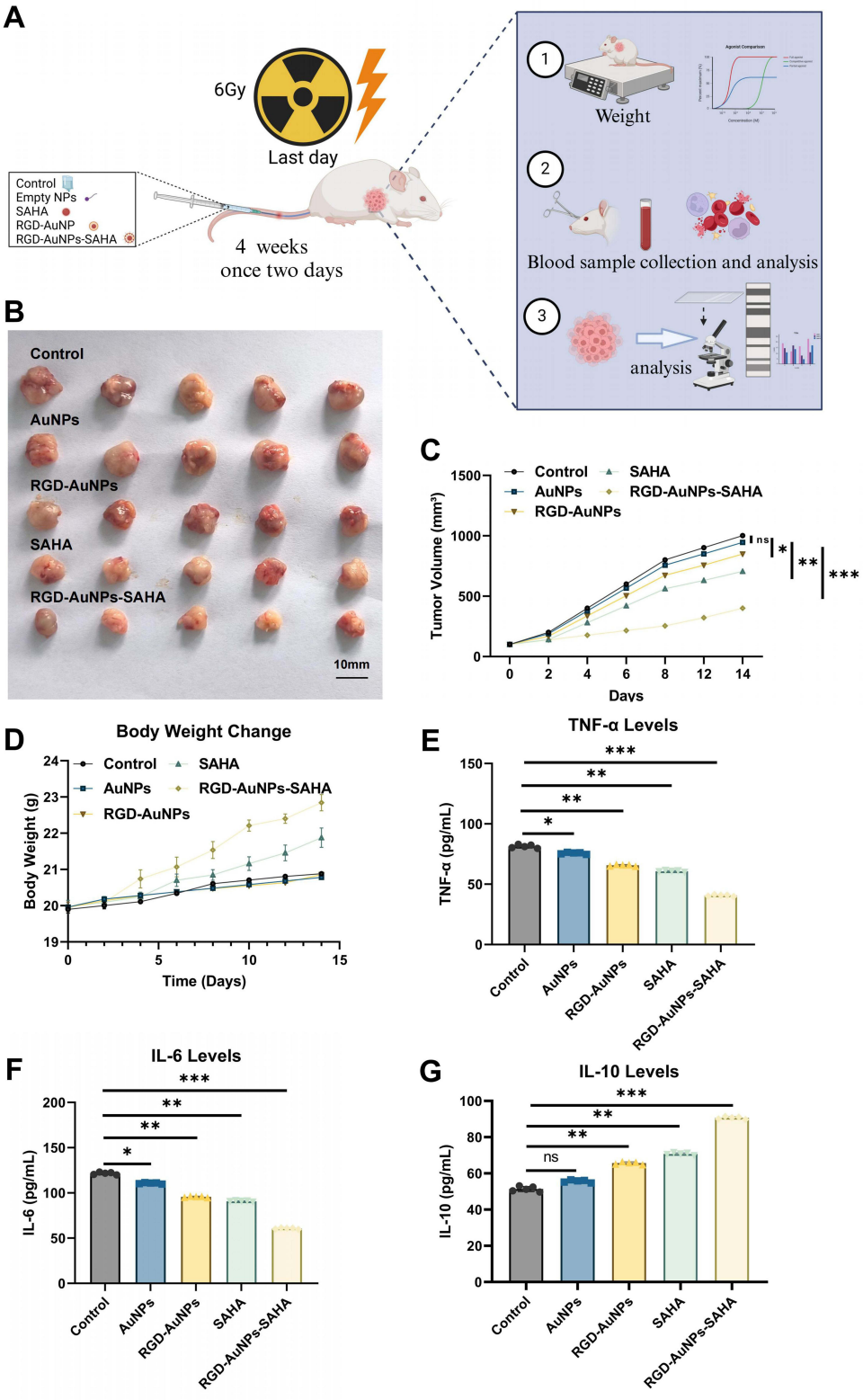

Figure 8 Effects of RGD-AuNPs-SAHA on Tumor Volume and Inflammatory Cytokine Levels.

Note: (**A**) Schematic diagram of the in vivo experimental design; (**B**) Tumor volume changes in mice across different treatment groups; (**C**) Percentage reduction in tumor volume in each group on day 14 of drug treatment; (**D**) Changes in body weight of mice during the drug treatment period; (**E**) Serum levels of TNF-α in different treatment groups; (**F**) Serum levels of IL-6 in different treatment groups; (**G**) Serum levels of IL-10 in different treatment groups. n=5. *p*-values between groups are as indicated in the figure ***$p<0.001$, **$p<0.01$, *$p<0.05$, ns indicates no significant difference ($p>0.05$).

https://doi.org/10.2147/IJN.S531731

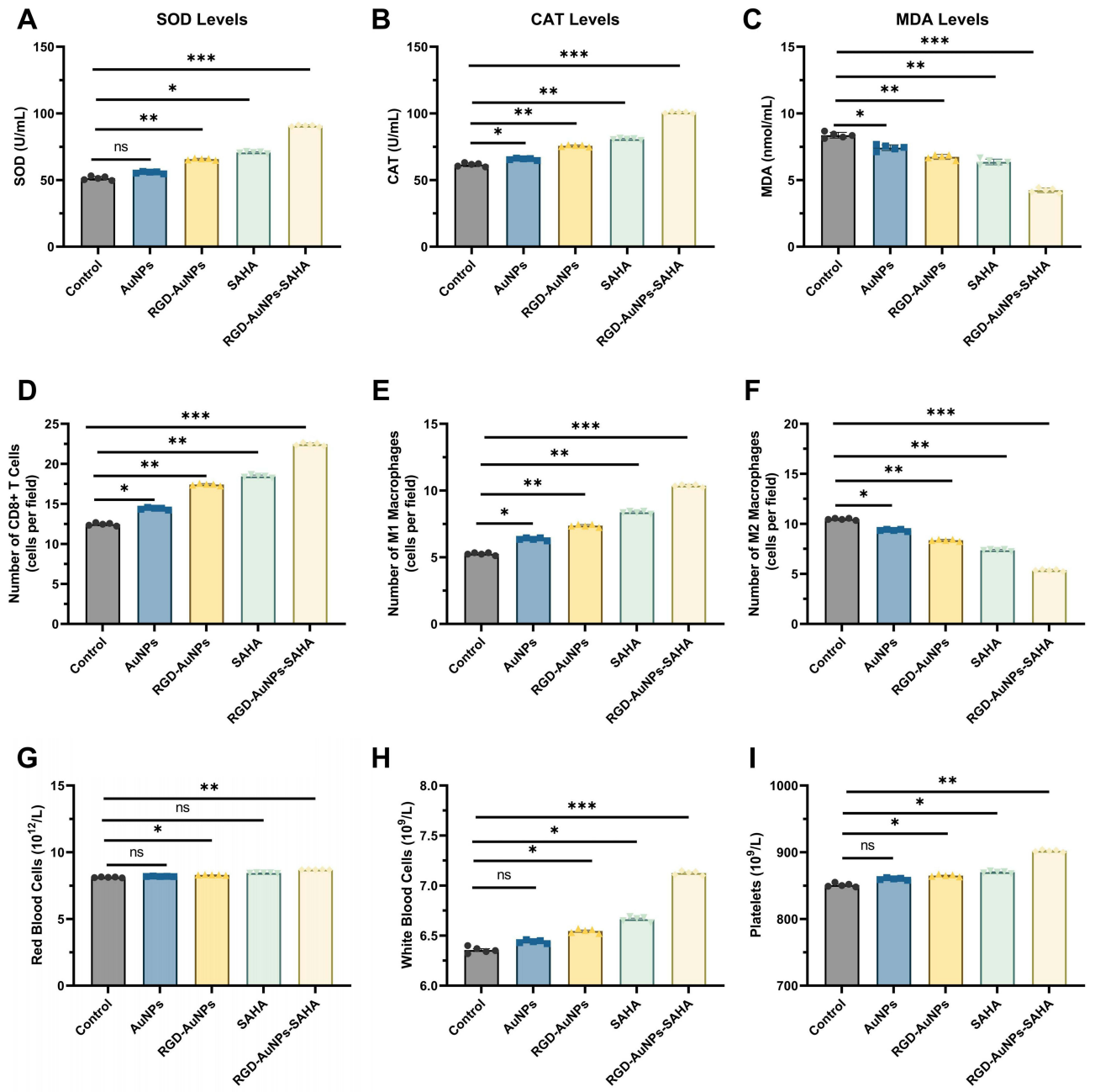

Figure 9 Effects of RGD-AuNPs-SAHA on Oxidative Stress and the Tumor Immune Microenvironment in Mice.
Note: (**A**) Bar graph showing serum SOD levels in different treatment groups; (**B**) Bar graph showing serum CAT levels in different treatment groups; (**C**) Bar graph showing serum MDA levels in different treatment groups; (**D**) Bar graph showing the number of $CD8^+$ T cells in tumor tissues of different treatment groups; (**E**) Bar graph showing the number of M1 macrophages in tumor tissues of different treatment groups; (**F**) Bar graph showing the number of M2 macrophages in tumor tissues of different treatment groups; (**G**) Bar graph showing the number of red blood cells in different treatment groups; (**H**) Bar graph showing the number of white blood cells in different treatment groups; (**I**) Bar graph showing the number of platelets in different treatment groups. n = 5, *p*-values are shown in the figure *** indicates $p < 0.001$, ** indicates $p < 0.01$, * indicates $p < 0.05$, and ns indicates no significant difference ($p > 0.05$).

group were minimal. In the SAHA group, there was a significant increase in all cell types, indicating a stimulatory effect of SAHA on the hematopoietic system. The RGD-AuNPs group also showed an increase in cell counts, but this was less pronounced than in the SAHA group, indicating limited efficacy of RGD-AuNPs alone. The most significant changes were observed in the RGD-AuNPs-SAHA group, where all cell types were significantly elevated, surpassing all other groups. This demonstrates that the combination of RGD-AuNPs-SAHA has the most pronounced effect on improving blood cell counts. These results suggest that RGD-AuNPs-SAHA not only exhibits significant tumor-suppressive effects

but also promotes the generation of red blood cells, white blood cells, and platelets, highlighting its potential for clinical application.

This study evaluated the effects of RGD-AuNPs-SAHA on oxidative stress and the tumor immune microenvironment in mice. The results revealed that the RGD-AuNPs-SAHA treatment increased the SOD and CAT levels while reducing MDA levels, thereby enhancing antioxidant capacity. Flow cytometry analysis demonstrated a marked increase in the number of $CD8^+$ T cells and M1 macrophages, coupled with a reduction in M2 macrophages, thereby enhancing the tumor immune response. Additionally, complete blood counts showed a significant increase in red blood cells, white blood cells, and platelets in the RGD-AuNPs-SAHA group, indicating a stimulatory effect on the hematopoietic system. Overall, RGD-AuNPs-SAHA exhibited notable effects in anti-tumor activity, antioxidation, and hematopoiesis, suggesting promising clinical application potential.

RGD-AuNPs-SAHA Significantly Inhibits Hypoxia Signaling Pathways and Enhances Tumor Cell Apoptosis Following Radiation Therapy

IHC analysis revealed that HIF-1α and VEGF expression in tumor tissues was significantly decreased in the RGD-AuNPs -SAHA group (Figure 10A), indicating effective suppression of tumor hypoxia and angiogenesis. In contrast, the control and AuNP-only groups showed high expression levels, with no significant difference between them. SAHA and RGD-AuNPs treatments led to moderate reductions, but these were markedly less pronounced than those observed with RGD-AuNPs-SAHA, emphasizing the enhanced hypoxia-modulating effect of the combined formulation (Figure 10B).

These findings indicate that RGD-AuNPs-SAHA not only significantly inhibits tumor growth but also effectively improves the tumor hypoxic microenvironment, thereby providing a theoretical basis for enhancing the sensitivity of NSCLC to radiation therapy.

Western blotting and RT-qPCR were conducted to assess the expression of hypoxia-related genes and proteins in tumor tissues. The RGD-AuNPs-SAHA group showed a marked reduction in both HIF-1α and VEGF protein levels (Figure 10C). Specifically, RT-qPCR analysis revealed that mRNA levels of HIF-1α and VEGF decreased (Figure 10D), which was corroborated by Western blot showing a substantial decrease in the corresponding protein levels.

When assessing apoptosis in tumor cells post-RT using apoptosis assays (live/dead staining), we observed a markedly higher proportion of apoptotic cells in the RGD-AuNPs-SAHA group compared to the other groups (Figure 10E). Quantitative data indicated that the apoptotic cell ratio increased in the RGD-AuNPs-SAHA group (Figure 10F). Additionally, γ-H2AX staining for DNA damage revealed elevated γ-H2AX expression levels in the RGD-AuNPs-SAHA group, suggesting an enhanced DNA damage response (Figure 10G). Specifically, the apoptotic cell ratio increased by about 71%, and the proportion of γ-H2AX-positive cells increased by approximately 67% in the RGD-AuNPs-SAHA group (Figure 10H).

These findings demonstrate that RGD-AuNPs-SAHA not only significantly inhibits the hypoxia signaling pathway in tumors but also enhances apoptosis and DNA damage response following RT, thereby increasing the radiosensitivity of NSCLC.

Preclinical Evaluation of RGD-AuNPs-SAHA Using PDTOs

Organoids have recently emerged as robust preclinical models that closely replicate the original clinical tumor architecture, cellular heterogeneity, and transcriptomic profiles.[30,35] To accelerate clinical translation of RGD-AuNPs-SAHA, we established PDTOs from resected NSCLC tissues. As shown in Figure 11A, PDTOs exhibited either solid or cystic morphologies under bright-field microscopy, likely reflecting heterogeneity among patient samples.

To determine whether RGD-AuNPs-SAHA exerts direct cytotoxic effects on PDTOs, we treated organoids with AuNPs, SAHA, RGD-AuNPs, or RGD-AuNPs-SAHA. CCK-8 assay results (Figure 11B) showed that both SAHA and RGD-AuNPs-SAHA significantly reduced organoid viability compared to the control and unloaded nanoparticle groups, with the greatest inhibitory effect observed in the RGD-AuNPs-SAHA group. Flow cytometry analysis further demonstrated increased apoptosis in SAHA- and RGD-AuNPs-SAHA-treated groups, with the highest proportion of apoptotic

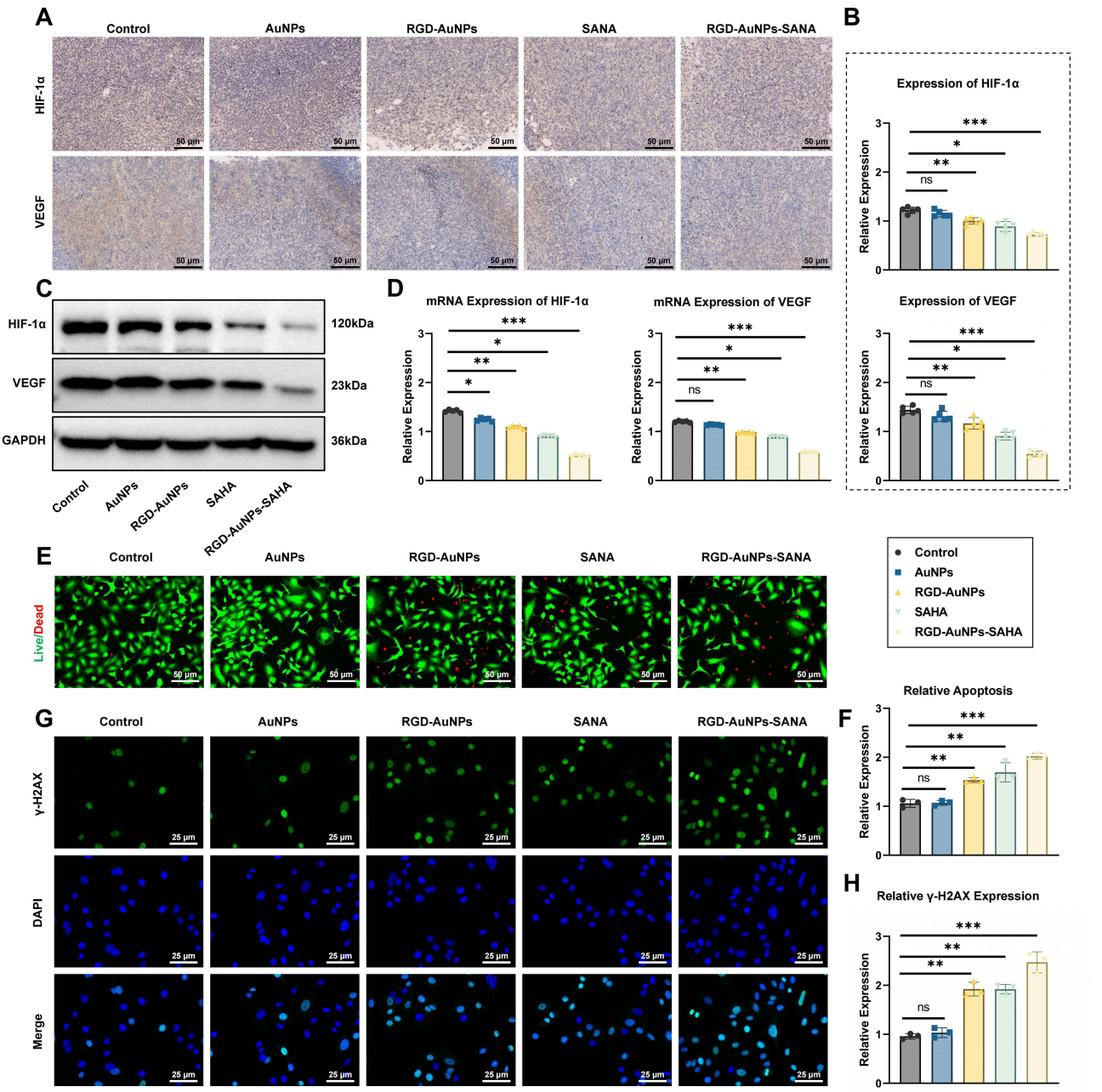

Figure 10 Effects of RGD-AuNPs-SAHA on Hypoxia Signaling Pathway and Cell Apoptosis.

Note: (**A**) IHC staining of tumor tissues for HIF-1α and VEGF expression levels, scale bar = 50 μm; (**B**) Quantitative analysis of IHC results showing a significant reduction in HIF-1α and VEGF expression in the RGD-AuNPs-SAHA group; (**C**) Western blot analysis of HIF-1α and VEGF protein expression in tumor tissues; (**D**) RT-qPCR analysis of HIF-1α and VEGF mRNA expression in tumor tissues; (**E**) Apoptosis detection (live/dead staining) showing the proportion of apoptotic tumor cells in each group, scale bar = 100 μm; (**F**) Quantitative analysis of apoptosis detection showing a significant increase in the proportion of apoptotic cells in the RGD-AuNPs-SAHA group; (**G**) γ-H2AX IF staining to assess DNA damage, scale bar = 100 μm; (**H**) Quantitative analysis of γ-H2AX positive cells showing a significant increase in DNA damage response in the RGD-AuNPs-SAHA group. n=5, *p* values are indicated in the figure ***$p<0.001$, **$p<0.01$, *$p<0.05$, ns indicates no significant difference ($p>0.05$).

cells seen in the RGD-AuNPs-SAHA group (Figure 11C). These results indicate that RGD-AuNPs-SAHA effectively suppresses organoid growth and promotes apoptosis in vitro.

RT-qPCR and ELISA were employed to detect hypoxia-related markers in PDTOs. HIF-1α and VEGF levels were decreased in the SAHA, RGD-AuNPs, and RGD-AuNPs-SAHA groups relative to the control and unloaded AuNP groups, with the strongest inhibition observed in the RGD-AuNPs-SAHA group (Figure 11D and E), suggesting effective remodeling of the hypoxic microenvironment by the nanocomplex.

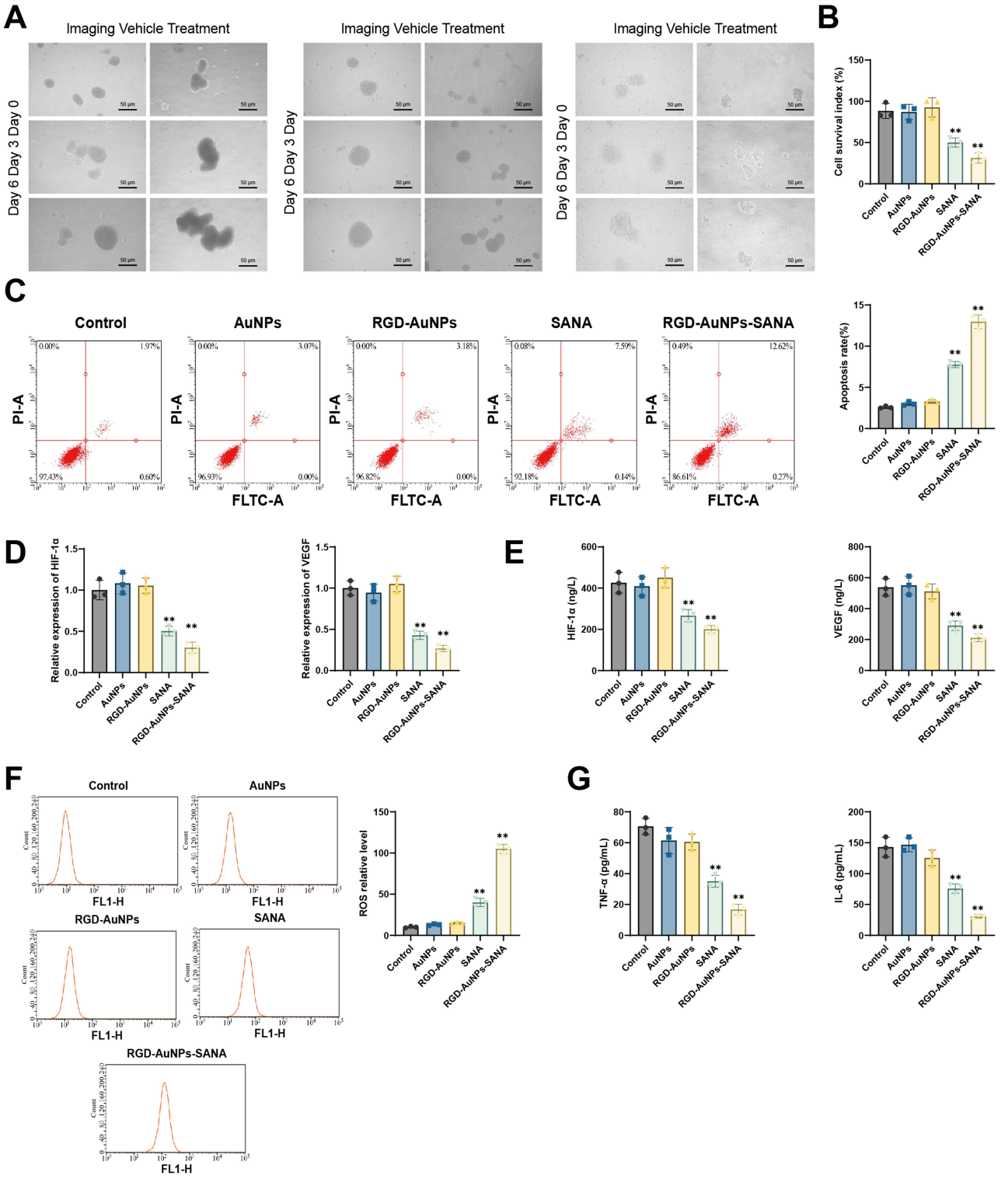

Figure 11 Evaluation of RGD-AuNPs-SAHA efficacy in PDTOs.

Note: (**A**) Representative bright-field images of PDTOs derived from clinical NSCLC samples. Scale bar = 100 μm; (**B**) CCK-8 assay to evaluate PDTO cell viability; (**C**) Flow cytometry analysis of Calu-1 and A549 cell apoptosis following 24 h treatment, using Annexin V-FITC and PI staining. Right panel: quantitative analysis of apoptotic PDTOs; (**D**) RT-qPCR analysis of HIF-1α and VEGF mRNA levels in each group; (**E**) ELISA quantification of HIF-1α and VEGF protein levels; (**F**) Flow cytometry detection of intracellular ROS accumulation; (**G**) ELISA detection of TNF-α and IL-6 protein levels in PDTOs. Unless otherwise specified, all experiments were performed in triplicate (n = 3). $^{**}p < 0.01$.

https://doi.org/10.2147/IJN.S531731

To further investigate oxidative stress, intracellular ROS levels were measured. As shown in Figure 11F, the RGD-AuNPs-SAHA group exhibited the highest ROS accumulation, indicating strong induction of oxidative stress in the tumor organoids.

We also assessed inflammatory responses by measuring pro-inflammatory cytokines in the culture supernatants. ELISA results showed that TNF-α and IL-6 levels were lower in the RGD-AuNPs-SAHA group compared to all other groups (Figure 11G), indicating an effective anti-inflammatory effect.

Together, these data are consistent with our prior in vitro and in vivo findings, confirming that RGD-AuNPs-SAHA suppresses hypoxia signaling, reduces cell viability, increases ROS generation, and promotes apoptosis in NSCLC-derived organoids. These findings strongly support its potential for clinical translation.

Discussion

NSCLC is one of the most common types of lung cancer globally. However, the tumor hypoxic microenvironment significantly reduces the effectiveness of radiation therapy.[36,37] Recently, nanotechnology has gained attention for its potential in anti-tumor drug delivery. AuNPs have emerged as promising carriers owing to their excellent biocompatibility and ease of modification.[38,39] RGD peptides can target integrin receptors in tumors, enhancing the precision of drug delivery.[40] This study innovatively proposes using RGD-modified AuNPs to deliver SAHA to improve radiation therapy outcomes for NSCLC. The RGD-AuNPs-SAHA complex significantly increases drug accumulation in tumors through targeted delivery and enhances radiation sensitivity by modulating the hypoxic microenvironment and inflammatory responses, demonstrating superior advantages over traditional drug delivery systems.

The results of this study further confirm SAHA's role in regulating tumor hypoxia signaling pathways. The hypoxic microenvironment is a critical contributor to tumor progression and resistance to RT. Previous research has identified HIF-1α as a central molecule in the regulation of tumor hypoxia, with SAHA modulating the hypoxic microenvironment by inhibiting HIF-1α expression.[41] While most studies have focused on systemic delivery of SAHA, this study utilized nanoparticles as carriers for SAHA, significantly enhancing the drug's accumulation at tumor sites and thereby improving its effect on the hypoxic microenvironment. Experimental results demonstrate that RGD-AuNPs-SAHA significantly reduces the expression of HIF-1α and VEGF in tumor tissues, indicating that this complex effectively alleviates the hypoxic microenvironment and further reduces tumor growth and spread by inhibiting angiogenesis.

Oxidative stress plays a critical role in tumor initiation and progression,[42,43] and our study demonstrates that RGD-AuNPs-SAHA significantly reduces oxidative stress levels in NSCLC tumors. Previous research has reported that tumor cells often exhibit elevated levels of ROS, which can promote genetic mutations and cancer progression. By reducing ROS levels, SAHA can potentially slow tumor development. However, conventional SAHA treatment is often limited by the tumor microenvironment, diminishing its antioxidant effects. In this study, the antioxidant effect of SAHA was enhanced through an RGD-modified AuNPs delivery system. Experimental results showed that the compound significantly reduced MDA levels and markedly increased the activity of antioxidant enzymes such as SOD and CAT. These findings further support the potential of SAHA in mitigating oxidative stress, especially when used in combination with nanodrug delivery systems to optimize its efficacy.

In addition, this study investigated the effects of RGD-AuNPs-SAHA on tumor cell apoptosis and DNA damage using TUNEL and γ-H2AX staining assays. As a histone deacetylase (HDAC) inhibitor, SAHA primarily functions by promoting histone acetylation, thereby inducing cell cycle arrest and apoptosis. Previous studies have confirmed that SAHA can effectively induce apoptosis in a variety of tumor cells; however, its role in mediating DNA damage responses has been relatively underexplored.[44] Our findings demonstrate that RGD-AuNPs-SAHA not only significantly increased apoptosis in A549 cells but also enhanced DNA damage response by upregulating the DNA damage marker γ-H2AX. These results further reveal the potential of SAHA to enhance radiosensitization through multiple mechanisms, with the effect being further amplified by the synergistic action of the nanoparticle delivery system.

In addition to regulating oxidative stress, this study is the first to systematically explore the role of SAHA in modulating the inflammatory response in NSCLC. Previous research has primarily focused on the direct effects of SAHA on tumor cell proliferation and apoptosis, with limited investigation into its influence on inflammation within the tumor microenvironment.[45] By analyzing the levels of pro-inflammatory cytokines (TNF-α and IL-6) and the anti-inflammatory

cytokine (IL-10), our study found that RGD-AuNPs-SAHA significantly inhibited pro-inflammatory responses and enhanced anti-inflammatory effects. Compared to SAHA alone, the RGD-AuNPs-SAHA complex was more effective in reducing pro-inflammatory cytokines and increasing anti-inflammatory cytokines. These findings suggest that RGD-AuNPs-SAHA not only acts directly on tumor cells but also modulates the inflammatory response to improve the tumor microenvironment, thereby further enhancing the efficacy of RT.

It is worth noting that although our study addressed the therapeutic relevance of oxidative stress, DNA damage response (DDR), and inflammatory pathways, a comprehensive elucidation of their underlying mechanisms is still lacking. Reactive oxygen species (ROS), as major cellular stress mediators in tumors, are typically generated upon exposure to exogenous insults such as ionizing radiation (IR), chemotherapeutic agents, and environmental stressors. These ROS are produced primarily from mitochondria, endoplasmic reticulum, NADPH oxidases, and peroxisomal enzymes.[46–49] On one hand, ROS can oxidize protein thiol groups to modulate protein structure and function, thereby acting as intracellular signaling messengers. On the other hand, ROS can nonspecifically damage various biomolecules, including DNA, and disrupt critical cellular processes such as cell cycle progression, motility, and survival.[46,50,51] As a well-established mediator of DNA damage, ROS can induce DNA double-strand breaks (DSBs) in tumor cells, subsequently activating the DDR network, which determines cell fate through DNA repair, apoptosis, or immune clearance.[52] It has been reported that ROS may exert these effects via several signaling pathways, including NF-κB, MAPKs, Keap1-Nrf2-ARE, and PI3K-Akt.[46,53] These observations support a cascade model in which ROS induces DNA damage, leading to subsequent apoptosis and other downstream effects. Phosphorylated H2AX (γH2AX) is widely recognized as a biomarker of DNA damage and plays a pivotal role in regulating cell fate decisions such as apoptosis and survival.[54,55] γH2AX facilitates the recruitment of DDR components to DSB sites, initiating the repair process,[56,57] and is therefore considered a rapid and sensitive indicator of DSB repair activity.[58] Interestingly, the relationship between ROS and γH2AX is bidirectional. While ROS can induce DNA damage marked by γH2AX, γH2AX itself can regulate ROS production through activation of the Nox1-Rac1 complex.[59–61] However, the specific molecular mechanisms by which ROS induces DNA damage and triggers apoptosis, as well as the signaling pathways involved in SAHA- and RGD-AuNPs-mediated enhancement of DDR and inflammation regulation in NSCLC, remain unclear. These questions warrant further investigation using high-throughput sequencing approaches integrated with molecular biology validation strategies, which are currently being planned for our future studies.

Compared with previous studies, this research introduces innovations in the selection of RGD peptide modification and the loading strategy of AuNPs. Through systematic in vitro and in vivo experiments, we comprehensively evaluated the radiosensitizing effects of the complex. While other studies have explored the combination of SAHA with nanoparticles, the incorporation of RGD peptides in this study significantly enhanced targeting and delivery efficiency, resulting in improved drug accumulation and efficacy within tumors. Moreover, we conducted multi-level experimental analyses to investigate the mechanisms of this complex in relation to the hypoxic tumor microenvironment, oxidative stress, inflammatory response, apoptosis, and DNA damage, offering novel insights into the application of nanomedicine in cancer therapy.

In summary, this study successfully developed and validated an RGD-modified AuNPs-SAHA complex, which significantly improved the radiosensitivity of NSCLC by reshaping the tumor hypoxic microenvironment, reducing oxidative stress, and modulating the inflammatory response (Figure 12). The complex demonstrated excellent antitumor activity in vitro and exhibited notable efficacy in mouse models. Despite these promising results, further evaluation of the long-term safety and biocompatibility of this nanosystem is needed for clinical application. Future research could also explore its potential in other tumor types and enhance its therapeutic efficacy by combining it with treatments such as immunotherapy.

Conclusion

In this study, we successfully synthesized RGD-AuNPs-SAHA and comprehensively evaluated their role in remodeling the tumor hypoxic microenvironment and enhancing the radiosensitivity of NSCLC. Our results demonstrated that RGD-AuNPs-SAHA exhibited excellent stability and biocompatibility both in vitro and in vivo, and efficiently penetrated A549 tumor cells. Through a series of cellular and animal experiments, we found that RGD-AuNPs-SAHA significantly

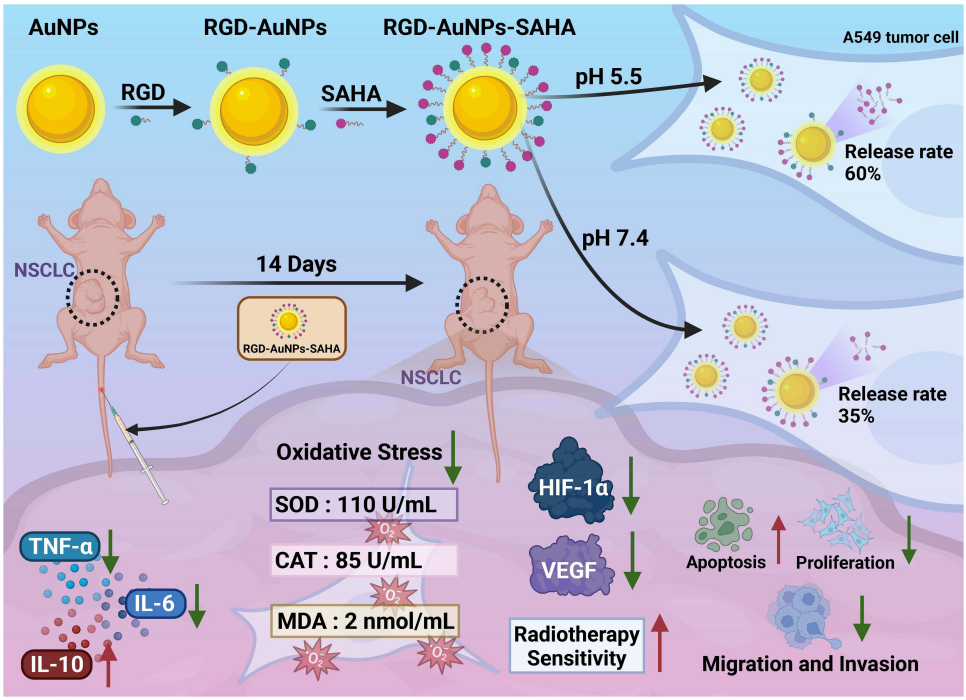

Figure 12 Schematic of how RGD-modified gold nanoparticles loaded with SAHA (RGD-AuNPs-SAHA) remodel the hypoxic–inflammatory tumor microenvironment to enhance radiosensitivity in NSCLC.

inhibited tumor cell proliferation, migration, and invasion, while increasing apoptosis rates. Furthermore, RGD-AuNPs-SAHA effectively suppressed tumor growth in vivo. Importantly, it also reduced the expression of HIF-1α and VEGF in the tumor hypoxic microenvironment, thereby enhancing the tumor's sensitivity to RT.

This study not only reveals the potential mechanisms of the RGD-AuNPs-SAHA complex in cancer treatment from a fundamental research perspective but also highlights its significant potential for clinical application. By improving the tumor microenvironment, RGD-AuNPs-SAHA significantly enhances the efficacy of RT, positioning it as a promising and effective adjunctive therapy for NSCLC. Its excellent biocompatibility and efficient drug release properties give it considerable advantages for future clinical translation.

Despite these promising results, the study has some limitations. First, the research mainly focuses on in vitro experiments and mouse models, necessitating further validation of its efficacy and safety in larger preclinical animal models and human clinical trials. Second, the potential of RGD-AuNPs-SAHA in other types of tumors has not been fully explored. Additionally, more comprehensive studies are needed to assess the long-term metabolism and potential toxicity of nanoparticles in vivo.

Future research should aim to optimize the preparation process of nanoparticles, enhance their drug loading efficiency and targeting capability, and explore their application in a wider range of tumor therapies. Large-scale, multicenter clinical trials are essential to validate their efficacy and safety, ultimately advancing their clinical use in cancer treatment.

Abbreviations

ALT, Alanine Aminotransferase; ANOVA, Analysis of Variance; AST, Aspartate Aminotransferase; AuNPs, Gold Nanoparticles; BUN, Blood Urea Nitrogen; CAT, Catalase; CREA, Creatinine; DCFH-DA, 2′,7′-Dichlorodihydrofluorescein Diacetate; DLS, Dynamic Light Scattering; ELISA, Enzyme-Linked Immunosorbent Assay; FBS, Fetal Bovine Serum; FTIR, Fourier Transform Infrared Spectroscopy; H&E, Hematoxylin and Eosin; HIF, Hypoxia-Inducible Factor; HPLC, High-Performance Liquid Chromatography; IHC, Immunohistochemistry; IF, Immunofluorescence; IL-6, Interleukin-6; MDA, Malondialdehyde; NSCLC, Non-Small Cell Lung Cancer; PI,

Propidium Iodide; RGD-AuNPs, RGD Peptide-Modified Gold Nanoparticles; RGD-AuNPs-SAHA, RGD Peptide-Modified Gold Nanoparticles Loaded with Suberoylanilide Hydroxamic Acid; ROS, Reactive Oxygen Species; RT, Radiotherapy; RT-PCR, Reverse Transcription Polymerase Chain Reaction; SAHA, Suberoylanilide Hydroxamic Acid; SOD, Superoxide Dismutase; TGA, Thermogravimetric Analysis; TEM, Transmission Electron Microscope or Transmission Electron Microscopy; TNF-α, Tumor Necrosis Factor-Alpha; UV-Vis, Ultraviolet-Visible Spectrophotometer; VEGF, Vascular Endothelial Growth Factor.

Ethical Statement

This study was approved by the Ethics Committee of People's Hospital of Longhua Shenzhen (2023-026-01). All animal experiments were performed in accordance with the Animal Care and Use Guidelines of the Ethics Committee of People's Hospital of Longhua Shenzhen, and in compliance with the internationally recognized guidelines for the care and use of laboratory animals.

Author Contributions

All authors made a significant contribution to the work reported, whether that is in the conception, study design, execution, acquisition of data, analysis and interpretation, or in all these areas; took part in drafting, revising or critically reviewing the article; gave final approval of the version to be published; have agreed on the journal to which the article has been submitted; and agree to be accountable for all aspects of the work.

Funding

This work was supported by Scientific research project of medical and health institutions in Longhua District, Shenzhen (2022011, 2023009).

Disclosure

The authors declare no conflicts of interest in this work.

Data Sharing Statement

The original contributions presented in the study are included in the article/supplementary materials, further inquiries can be directed to the corresponding authors.

References

1. Jani CT, Singh H, Abdallah N, et al. Trends in Lung Cancer Incidence and Mortality (1990–2019) in the United States: a Comprehensive Analysis of Gender and State-Level Disparities. *JCO Glob Oncol*. 2023;9. doi:10.1200/go.23.00255
2. Ganti AK, Klein AB, Cotarla I, Seal B, Chou E. Update of incidence, prevalence, survival, and initial treatment in patients with non–small cell lung cancer in the US. *JAMA Oncol*. 2021;7(12):1824. doi:10.1001/jamaoncol.2021.4932
3. Ichi WS, Yotsukura M, Miyoshi T, et al. Updated review of perioperative treatment for non-small-cell lung cancer in the new era of immune checkpoint inhibitors: past, present, and future. *Japanese J Clin Oncol*. 2024;54(12):1244–1253. doi:10.1093/jjco/hyae106
4. PDQ Adult Treatment Editorial Board. Non-Small Cell Lung Cancer Treatment (PDQ®): Health Professional Version. In: *PDQ Cancer Information Summaries*. National Cancer Institute (US); 2025.
5. Zhou C, Li M, Wang Z, An D, Li B. Adverse events of immunotherapy in non-small cell lung cancer: a systematic review and network meta-analysis. *Int Immunopharmacol*. 2022;102:108353. doi:10.1016/j.intimp.2021.108353
6. Césaire M, Montanari J, Curcio H, et al. Radioresistance of non-small cell lung cancers and therapeutic perspectives. *Cancers*. 2022;14(12):2829. doi:10.3390/cancers14122829
7. Zhao L, Li M, Shen C, et al. Nano-assisted radiotherapy strategies: new opportunities for treatment of non-small cell lung cancer. *Research*. 2024;7. doi:10.34133/research.0429
8. Zhang Y, Guo F, Wang Y. Hypoxic tumor microenvironment: destroyer of natural killer cell function. *Chin J Cancer Res*. 2024;36(2):138–150. doi:10.21147/j.issn.1000-9604.2024.02.04
9. Zhao Y, Liang C, Mei Z, et al. Oxygen-enriched MOF-hemoglobin X-ray nanosensitizer for enhanced cancer radio–radiodynamic therapy. *ACS Materials Lett*. 2023;5(12):3237–3247. doi:10.1021/acsmaterialslett.3c01158
10. Twigger SA, Dominguez B, Porto V, et al. The activity of therapeutic molecular cluster Ag5 is dependent on oxygen level and HIF-1 mediated signalling. *Redox Biol*. 2024;76:103326. doi:10.1016/j.redox.2024.103326
11. Bui BP, Nguyen PL, Lee K, Cho J. Hypoxia-inducible factor-1: a novel therapeutic target for the management of cancer, drug resistance, and cancer-related pain. *Cancers*. 2022;14(24):6054. doi:10.3390/cancers14246054

12. Vasileiou M, Tsianava C, Charalampos Diamantoudis S, Mazneva T, Giortsiou K. Opportunities and challenges of integrating HIF-1 into clinical practice for cancer treatment. *GPD*. 2024;3(2):3431. doi:10.36922/gpd.3431
13. Wicks EE, Semenza GL. Hypoxia-inducible factors: cancer progression and clinical translation. *J Clin Investig*. 2022;132(11). doi:10.1172/jci159839
14. Muz B, de la Puente P, Azab F, Azab AK. The role of hypoxia in cancer progression, angiogenesis, metastasis, and resistance to therapy. *Hypoxia*. 2015;83. doi:10.2147/hp.s93413
15. Alnasraui AHF, Joe IH, Al-Musawi S. Investigation of folate-functionalized magnetic-gold nanoparticles based targeted drug delivery for liver: in vitro, in vivo and docking studies. *ACS Biomater Sci Eng*. 2024;10(10):6299–6313. doi:10.1021/acsbiomaterials.4c01039
16. Seku K, Bhagavanth Reddy G, Osman AI, et al. Modified frankincense resin stabilized gold nanoparticles for enhanced antioxidant and synergetic activity in in-vitro anticancer studies. *Int J Biol Macromol*. 2024;278:134935. doi:10.1016/j.ijbiomac.2024.134935
17. Joseph J, Chandrasekaran R, Palani S. Anti-proliferative activities of Carthamidin mediated gold nanoparticles against breast cancer: an in-vitro approach. *Nano-Struct Nano-Objects*. 2024;39:101324. doi:10.1016/j.nanoso.2024.101324
18. Wang Z, Dong J, Zhao Q, et al. Gold nanoparticle-mediated delivery of paclitaxel and nucleic acids for cancer therapy (Review). *Mol Med Rep*. 2020;22(6):4475–4484. doi:10.3892/mmr.2020.11580
19. Qin W, Chandra J, Abourehab MAS, et al. New opportunities for RGD-engineered metal nanoparticles in cancer. *Mol Cancer*. 2023;22(1). doi:10.1186/s12943-023-01784-0
20. Roy R, Ria T, RoyMahaPatra D, Sk UH. Single inhibitors versus dual inhibitors: role of HDAC in cancer. *ACS Omega*. 2023;8(19):16532–16544. doi:10.1021/acsomega.3c00222
21. Xu J, Sun J, Wang P, Ma X, Li S. Pendant HDAC inhibitor SAHA derivatised polymer as a novel prodrug micellar carrier for anticancer drugs. *J Drug Targeting*. 2017;26(5–6):448–457. doi:10.1080/1061186x.2017.1419355
22. Li Z, Zhu WG. Targeting histone deacetylases for cancer therapy: from molecular mechanisms to clinical implications. *Int J Biol Sci*. 2014;10(7):757–770. doi:10.7150/ijbs.9067
23. Xing J, Wang H, Xu S, Han P, Xin M, Zhou JL. Sensitization of suberoylanilide hydroxamic acid (SAHA) on chemoradiation for human cervical cancer cells and its mechanism. *Eur J Gynaecol Oncol*. 2015;36(2):117–122.
24. Zhang N, Li J, Zhang P, Yang X, Sun C. Novel nanoarchitecture of arginine-glycine-aspartate conjugated gold nanoparticles: a sensitive and selective platform for detecting arachidonic acid. *Anal Bioanal Chem*. 2019;411(27):7105–7113. doi:10.1007/s00216-019-02092-7
25. Isakozawa S, Kaji K, Jarausch K, Terada S, Baba N. The development and characteristics of a high-speed EELS mapping system for a dedicated STEM. *J Electron Microscopy*. 2008;57(2):41–45. doi:10.1093/jmicro/dfn001
26. Potts JC, Jain A, Amabilino DB, Rawson FJ, Pérez-García L. Molecular surface quantification of multifunctionalized gold nanoparticles using UV–visible absorption spectroscopy deconvolution. *Anal Chem*. 2023;95(35):12998–13002. doi:10.1021/acs.analchem.3c01649
27. Robey RW, Shukla S, Steadman K, et al. Inhibition of ABCG2-mediated transport by protein kinase inhibitors with a bisindolylmaleimide or indolocarbazole structure. *Mol Cancer Ther*. 2007;6(6):1877–1885. doi:10.1158/1535-7163.mct-06-0811
28. Shi X, Karmali S, Sharma AM, Birch DW. A review of laparoscopic sleeve gastrectomy for morbid obesity. *OBES SURG*. 2010;20(8):1171–1177. doi:10.1007/s11695-010-0145-8
29. Sweegers MG, Buffart LM, Huijsmans RJ, et al. From accelerometer output to physical activity intensities in breast cancer patients. *J Sci Med Sport*. 2020;23(2):176–181. doi:10.1016/j.jsams.2019.09.001
30. Suvilesh KN, Manjunath Y, Nussbaum YI, et al. Targeting AKR1B10 by drug repurposing with epalrestat overcomes chemoresistance in non–small cell lung cancer patient-derived tumor organoids. *Clin Cancer Res*. 2024;30(17):3855–3867. doi:10.1158/1078-0432.ccr-23-3980
31. Ceccacci E, Minucci S. Inhibition of histone deacetylases in cancer therapy: lessons from leukaemia. *Br J Cancer*. 2016;114(6):605–611. doi:10.1038/bjc.2016.36
32. Bejarano L, Jordão MJC, Joyce JA. Therapeutic Targeting of the Tumor Microenvironment. *Cancer Discovery*. 2021;11(4):933–959. doi:10.1158/2159-8290.cd-20-1808
33. Emami Nejad A, Najafgholian S, Rostami A, et al. The role of hypoxia in the tumor microenvironment and development of cancer stem cell: a novel approach to developing treatment. *Cancer Cell Int*. 2021;21(1). doi:10.1186/s12935-020-01719-5
34. Hu J, Zhang L, Xia H, et al. Tumor microenvironment remodeling after neoadjuvant immunotherapy in non-small cell lung cancer revealed by single-cell RNA sequencing. *Genome Med*. 2023;15(1). doi:10.1186/s13073-023-01164-9
35. Shi R, Radulovich N, Ng C, et al. Organoid cultures as preclinical models of non–small cell lung cancer. *Clin Cancer Res*. 2020;26(5):1162–1174. doi:10.1158/1078-0432.ccr-19-1376
36. Sarma K, Akther MH, Ahmad I, et al. Adjuvant novel nanocarrier-based targeted therapy for lung cancer. *Molecules*. 2024;29(5):1076. doi:10.3390/molecules29051076
37. Li C, Hu M, Cai S, et al. Dysfunction of CD8+ T cells around tumor cells leads to occult lymph node metastasis in NSCLC patients. *Cancer Sci*. 2024;115(8):2528–2539. doi:10.1111/cas.16206
38. Virani NA, Kelada OJ, Kunjachan S, et al. Noninvasive imaging of tumor hypoxia after nanoparticle-mediated tumor vascular disruption. *PLoS One*. 2020;15(7):e0236245. doi:10.1371/journal.pone.0236245
39. Li XP, Hou DY, Wu JC, et al. Stimuli-Responsive Nanomaterials for Tumor Immunotherapy. *ACS Biomater Sci Eng*. 2024;10(9):5474–5495. doi:10.1021/acsbiomaterials.4c00388
40. Javid H, Oryani MA, Rezagholinejad N, Esparham A, Tajaldini M, Karimi-Shahri M. RGD peptide in cancer targeting: benefits, challenges, solutions, and possible integrin–RGD interactions. *Cancer Med*. 2024;13(2). doi:10.1002/cam4.6800
41. Ghosh R, Samanta P, Sarkar R, et al. Targeting HIF-1α by natural and synthetic compounds: a promising approach for anti-cancer therapeutics development. *Molecules*. 2022;27(16):5192. doi:10.3390/molecules27165192
42. Li K, Deng Z, Lei C, Ding X, Li J, Wang C. The role of oxidative stress in tumorigenesis and progression. *Cells*. 2024;13(5):441. doi:10.3390/cells13050441
43. Aboelella NS, Brandle C, Kim T, Ding ZC, Zhou G. Oxidative stress in the tumor microenvironment and its relevance to cancer immunotherapy. *Cancers*. 2021;13(5):986. doi:10.3390/cancers13050986
44. Huang H, Fu Y, Zhang Y, et al. Dissection of anti-tumor activity of histone deacetylase inhibitor SAHA in nasopharyngeal carcinoma cells via quantitative phosphoproteomics. *Front Cell Dev Biol*. 2020;8:8. doi:10.3389/fcell.2020.577784

45. Peng F, Liao M, Qin R, et al. Regulated cell death (RCD) in cancer: key pathways and targeted therapies. *Sig Transduct Target Ther*. 2022;7(1). doi:10.1038/s41392-022-01110-y
46. Zhang G, He J, Ye X, et al. β-Thujaplicin induces autophagic cell death, apoptosis, and cell cycle arrest through ROS-mediated Akt and p38/ERK MAPK signaling in human hepatocellular carcinoma. *Cell Death Dis*. 2019;10(4). doi:10.1038/s41419-019-1492-6
47. Meitzler JL, Antony S, Wu Y, et al. NADPH Oxidases: a Perspective on Reactive Oxygen Species Production in Tumor Biology. *Antioxid Redox Signaling*. 2014;20(17):2873–2889. doi:10.1089/ars.2013.5603
48. Fransen M, Nordgren M, Wang B, Apanasets O. Role of peroxisomes in ROS/RNS-metabolism: implications for human disease. *Biochimica et Biophysica Acta*. 2012;1822(9):1363–1373. doi:10.1016/j.bbadis.2011.12.001
49. Ziech D, Franco R, Pappa A, Panayiotidis MI. Reactive Oxygen Species (ROS)—Induced genetic and epigenetic alterations in human carcinogenesis. *Mutat Res*. 2011;711(1–2):167–173. doi:10.1016/j.mrfmmm.2011.02.015
50. Liou GY, Storz P. Reactive oxygen species in cancer. *Free Radical Res*. 2010;44(5):479–496. doi:10.3109/10715761003667554
51. Shi Y, Nikulenkov F, Zawacka-Pankau J, et al. ROS-dependent activation of JNK converts p53 into an efficient inhibitor of oncogenes leading to robust apoptosis. *Cell Death Differ*. 2014;21(4):612–623. doi:10.1038/cdd.2013.186
52. Srinivas US, Tan BWQ, Vellayappan BA, Jeyasekharan AD. ROS and the DNA damage response in cancer. *Redox Biol*. 2019;25:101084. doi:10.1016/j.redox.2018.101084
53. Zhang J, Wang X, Vikash V, et al. ROS and ROS-mediated cellular signaling. *Oxid Med Cell Longev*. 2016;2016(1). doi:10.1155/2016/4350965
54. Xiao A, Li H, Shechter D, et al. WSTF regulates the H2A.X DNA damage response via a novel tyrosine kinase activity. *Nature*. 2008;457 (7225):57–62. doi:10.1038/nature07668
55. Cook PJ, Ju BG, Telese F, Wang X, Glass CK, Rosenfeld MG. Tyrosine dephosphorylation of H2AX modulates apoptosis and survival decisions. *Nature*. 2009;458(7238):591–596. doi:10.1038/nature07849
56. Paull TT, Rogakou EP, Yamazaki V, Kirchgessner CU, Gellert M, Bonner WM. A critical role for histone H2AX in recruitment of repair factors to nuclear foci after DNA damage. *Curr Biol*. 2000;10(15):886–895. doi:10.1016/s0960-9822(00)00610-2
57. Rogakou EP, Pilch DR, Orr AH, Ivanova VS, Bonner WM. DNA double-stranded breaks Induce histone H2AX phosphorylation on Serine 139. *J Biol Chem*. 1998;273(10):5858–5868. doi:10.1074/jbc.273.10.5858
58. Rothkamm K, Löbrich M. Evidence for a lack of DNA double-strand break repair in human cells exposed to very low x-ray doses. *Proc Natl Acad Sci USA*. 2003;100(9):5057–5062. doi:10.1073/pnas.0830918100
59. Kang MA, So EY, Simons AL, Spitz DR, Ouchi T. DNA damage induces reactive oxygen species generation through the H2AX-Nox1/Rac1 pathway. *Cell Death Dis*. 2012;3(1):e249–e249. doi:10.1038/cddis.2011.134
60. Cheng G, Diebold BA, Hughes Y, Lambeth JD. Nox1-dependent reactive oxygen generation is regulated by Rac1. *J Biol Chem*. 2006;281 (26):17718–17726. doi:10.1074/jbc.m512751200
61. Mitsushita J, Lambeth JD, Kamata T. The superoxide-generating oxidase Nox1 is functionally required for Ras Oncogene transformation. *Cancer Res*. 2004;64(10):3580–3585. doi:10.1158/0008-5472.can-03-3909